Modeling and characterization of nanoelectromechanical systems

Martin Duemling

Thesis submitted to the Faculty of the
Virginia Polytechnic Institute and State University
in partial fulfillment of the requirements for the degree of

Masters of Science
in
Materials Science and Engineering

Dr. Stephane Evoy, Chair
Dr. James R. Heflin
Dr. William T. Reynolds, Jr.

August 15, 2002
Blacksburg, Virginia

Keywords: Nanotechnology, Nanomechanical resonator, NEMS

Modeling and characterization of nanoelectromechanical systems

Martin Duemling

(Abstract)

Microelectromechanical structures (MEMS) are used commercially in sensor applications and in recent years much research effort has been done to implement them in wireless communication. Electron beam lithography and other advancements in fabrication technology allowed to shrink the size of MEMS to nanomechanical systems (NEMS).

Since NEMS are just a couple of 100 nm in size, highly integrated sensor applications are possible. Since NEMS consume only little energy, this will allow continuous monitoring of all the important functions in hospitals, in manufacturing plants, on aircrafts, or even within the human body.

This thesis discusses the modeling of NEM resonators. Loss mechanisms of macroscale resonators, and how they apply to NEM resonators, will be reviewed. Electron beam lithography and the fabrication process of Silicon NEM resonator will be described. The emphasis of this work was to build a test setup for temperature dependant measurements. Therefore different feasible techniques to detect nanoscale vibration will be compared and the setup used in this work will be discussed. The successful detection of nanoscale vibration and preliminary results of the temperature dependence of the quality factor of a paddle resonator will be reported. A new approach to fabricate NEM resonator using electrofluidic assembly will be introduced.

To my wife

Acknowledgements

I would like to thank my advisor Dr. Stephane Evoy for his encouragement, guidance and support throughout the work, especially his continued support after he left Virginia Tech to join the University of Pennsylvania. Dr. James R. Heflin I thank for the space in his lab, his equipment and for handling all the money concerns after Dr. Evoy left. In addition I am thankful to my other committee member Dr. William T. Reynolds.

I would like to thank all the people who supported this work with their knowledge and time. Steve McCartney for teaching me electron microscopy, for his help in setting up the electron beam lithography tool and for giving me access to the microscope around the clock. Fred A. Mahone from the physics electronic shop for his quick response to my inquiries and for all the answers to my questions regarding the measurement equipment. Melvin Shaver, Scott Allen and John Miller from the physics machine shop for their help and input in building the setup. Dan Huff from the packaging lab for giving me access to the wirebonder. Dr. Hendricks and David Gray for the access to the clean room. Christopher Maxey for running the FEM simulation of the paddle resonators for me. Ben Hailer and Benjamin R. Martin, Thomas E. Mallouk, Irena Kratochvilova and Theresa S. Mayer from Penn State University for fabricating and assembling the rhodium NEMS. Anatoli Olkhovets and Harold Craighead from Cornell University for making silicon NEMS available to us to test our characterization setup. William D. Barnhart for the things he taught me regarding the silicon fabrication process. The particle physics group of Virginia Tech for their vacuum equipment and especially Mark Makela for his help with the equipment. Martin Drees for his help with the cryostat and other lab concerns. Ingrid Burbey and Martin Phelan for revising my thesis.

This work was funded by the electrical engineering departments of Virginia Tech and Upenn and by Oak Ridge National Laboratory and supported by the physics department of Virginia Tech.

Contents

List of figures

List of tables

1 Introduction

“There’s plenty of room at the Bottom” was the title of a talk given by Richard Feynman in December 1959 [1]. Since then many things he had envisioned have become true. Submicron circuits are commercially employed in computers. It is even possible to freely place single atoms on a substrate [2]. However, while there is still plenty of room at the bottom, there is even more in-between. In solid state physics, for example, as long as a system can be approximated as infinite, its behavior can be explained and predicted fairly well. At the other end systems consisting of a few electrons or an atom can be described by particle or molecular physics. In between these two regions lies the mesoscopic region, where the classical theories break down but where systems are already too large to apply straightforward quantum mechanics. In the mesoscopic region many questions remain unanswered. The best understood mesoscopic systems are electric systems (quantum dots, quantization of electrical conductance)[3]. Recently the first step to a theory of thermal conductance in the mesoscopic regime was reported [4]. But the mechanical behavior of mesoscopic system leaves many questions open. These questions will be addressed in this work.

1.1 Application of MEMS

The term MEMS (microelectromechanical structure) describes devices where a mechanical function is coupled with an electrical signal. These MEMS are used in a wide range of applications: from sensors using the change of resistance or capacitance [5], motors [6], applications for fluid transport [7], switches [8], phase shifters [9] or even optical switches in fiber communication [10]. A subgroup of MEMS are MEM resonators. These resonators are used in sensors [5] and in wireless communication [9]. Sensing functions can also be accomplished by monitoring changes in resonant frequency due to either forces on the resonator or through mass absorption. An example of a force sensor is an atomic force microscope (AFM) [11]. If the force between the atoms of the sample and the tip changes, so does the frequency of the resonator. An AFM has a resolution in the nano Newton range. In pressure sensors the force is due to the interaction of the surface with the surrounding gas [5]. The force on the resonator is pressure dependent and therefore pressure changes are accompanied by a change of the resonant frequency. Gas sensors are coated with an active layer that attracts certain gas molecules [12]. This additional mass changes also the resonant frequency. Since different molecules are absorbed by different coatings, gas sensors can be made for very specific gases. Biological sensors work in a similar way. There the resonator is coated with an immobilized antibody. These sensors achieve a sensitivity of a few cells [13]. While gas sensors are commercially available, biological sensors are still in development.

Angular acceleration can be measured with microgyrometers [5]. In a microgryrometer, a mass supported by a spring in the x and y direction, rotates around the z-axis. The amplitude of the x and y oscillation is proportional to the rotation around the z-axis.

Resonators can be used in wireless communication as filters [9], oscillators [9] and mixers [9]. A resonator will only resonate around its resonant frequency. This property is utilized in filters. In a filter the input signal is used to excite the resonator and the output signal is coupled to the amplitude response of the resonator. This way signals with frequencies away from the resonant frequency are filtered out. A resonator in connection with a feedback amplifier can be used as an oscillator. The output signal of an oscillator has the resonant frequency of the resonator. This signal can be used as a carrier frequency in wireless communication. A mixer has two input signals with two different frequencies and the output signal will be the sum of the signals but with another frequency [14]. So far MEM resonators are not used in wireless communication application. One of the main reasons for this is that the integration with the integrated circuitry (IC) is difficult. To integrate sensors the electronics are often built on one chip and the actual sensor on another, the two chips are than wirebonded together [16]. This method is not feasible for wireless communication, because the advantage of size reduction compared to quartz resonators would be lost. Also the frequency regime of MEM resonators limits their possible functions in wireless communication.

1.2 Nanoelectromechanical structures

Reducing the size of a resonator increases its resonant frequency. Since frequencies in the GHZ range are possible, NEM resonators are envisioned for RF or microwave communication. A consequence of the smaller mass of the resonator is that smaller changes in the mass can be detected, which enables an NEM resonator to detect masses approaching the level of single atoms [17]. Charges can also be detected with NEM resonators with an ultimate sensitivity of an electron [18].

Another possible application of NEM resonators is magnetic resonant force microscopy (MRFM) [17]. In MRFM the interaction of the intrinsic magnetic moment (spin) of a nuclei with an applied magnetic field is utilized. With today's technique (nuclear magnetic resonant spectrometry (NMR)) a response of $10^{14} - 10^{16}$ nuclei generates a measurable signal (which leads to a resolution of 10 μm). Sidles (1991) has shown theoretically that a sensitivity down to the spin of a single proton can be achieved with a mechanical detection method. If a nanomagnet is used to provide a magnetic field, it can vary so strongly in space that the nuclear resonant condition is satisfied only in the volume of an atom, a 3D mapping of individual biomolecules would be therfore possible. The tiny back action of the interaction of the spin with the external magnetic field results in a vibration of the cantilever. It is already possible to measure the magnitude of forces that result from a single resonant nucleus (10^{-18} N) [19].

Another interesting aspect of NEM resonators is that they allow research on quantum mechanical resonators. In the millikelvin range the thermal energy (kT) of a GHz range NEM resonator is in the order of the energy quantum (*hv)*. There the thermal fluctuations will be smaller than the intrinsic quantum noise. So the square amplitude of the vibration should be quantized, only having values that are multiples of hfQ/2 k_{eff}. Transducers that measure the position squared are only a factor 100 away from the sensitivity that is needed to measure displacement in the quantum domain (10^{-27} m^2) [20][17].

Another advantage of NEMS is their low energy consumption, even a million nanomechanical elements would dissipate only a millionth of a watt. This could lead to miniature sensors with low power consumption. Important functions in hospitals, in manufacturing plants, on aircrafts, or even within the human body could be continuously monitored with these sensors [21].

The size reduction also brings some major challenges. If the frequency is changed by a few additional atoms on the surface, it will be difficult to mass-produce resonators with the same properties. The communication with the macro world is already challenging in MEMS application and will increase further for NEMS devices: For example, a signal of the magnitude of a few electrons can get easily obscured by thermal vibration.

At present our understanding of nano mechanical systems is very limited. For example the quality factor of microelectromechanical (MEM) resonators is around 10^{11} at cryogenic temperatures, reducing the size of the resonator to a nano level decreases the quality factor to less than 10^7 [17]. Since the percentage of surface and near surface atoms increases with decreasing size, the decrease of the quality factor is probably surface related, but its precise origin is not known yet [17].

This work had three goals. The first goal was to setup an electron beam lithography tool and to develop a nanofabrication process. The second was to review existing vibration models and to develop an adequate model of the vibration of NEM resonators. The last and most important goal was to develop a test setup for temperature-dependent experimental testing of NEM resonators.

1.3 Overview of this thesis

The mechanical properties of NEM resonators will be discussed in chapter two. First the resonant frequency of the resonator is derived using elasticity and simple beam theory. Then it will be shown that these more complex mechanical systems can be approximated as simple harmonic oscillators. In chapter three and four the main mechanisms that contribute to energy dissipation in an NEM resonator will be discussed. Chapter three concentrates on the more general and fundamental loss mechanisms, while in chapter four relaxation phenomena are discussed. Chapter five describes the device fabrication and the experimental setup. In chapter six the results of the experiments are discussed. It will be shown that we were able to measure the resonant frequency and the quality factor of NEM resonators as a function of temperature. Chapter seven is dedicated to an alternative fabrication method based on the self-assembly of rhodium rods. Finally this work will conclude with a discussion of possible improvements of the setup (chapter eight) and further work that must be done to obtain a better understanding of NEM resonators (chapter nine).

2 Theory of vibration

For designing and modeling a device based on an NEM resonator, a theoretical understanding of its vibration is necessary. A theoretical understanding of vibration is also necessary for a correct interpretation of experimental data. In part 2.1.1, the resonant frequency of a cantilever beam will be derived using simple beam theory and elasticity. The remaining part of 2.1 will review approaches to overcome the limitation of the simple beam theory and how damping can be introduced into simple beam theory. In part 2.2, it will be shown that a resonator can be approximated as a simple harmonic oscillator. The model of a simple harmonic oscillator will than be used in part 2.3 to model the resonant behavior of paddle resonators.

2.1 Theory of elasticity of beams and cantilever

Simple beam-theory is restricted to a prismatic (equal cross section), homogeneous, straight and untwisted structure. The thickness (d) and width (w) have to be small compared to the length (l), which reduces the problem to an one-dimensional problem along the length of the beam. Furthermore it is assumed that the normal stresses (σ) in the x and y direction can be neglected [22]. The following derivation only holds if the maximum deflection (in x) is smaller than the radius of gyration (K). If the maximum deflection approaches K, additional non-linear terms must be considered [23]. The coordinate system used for the following derivation is shown in figure 2.1.

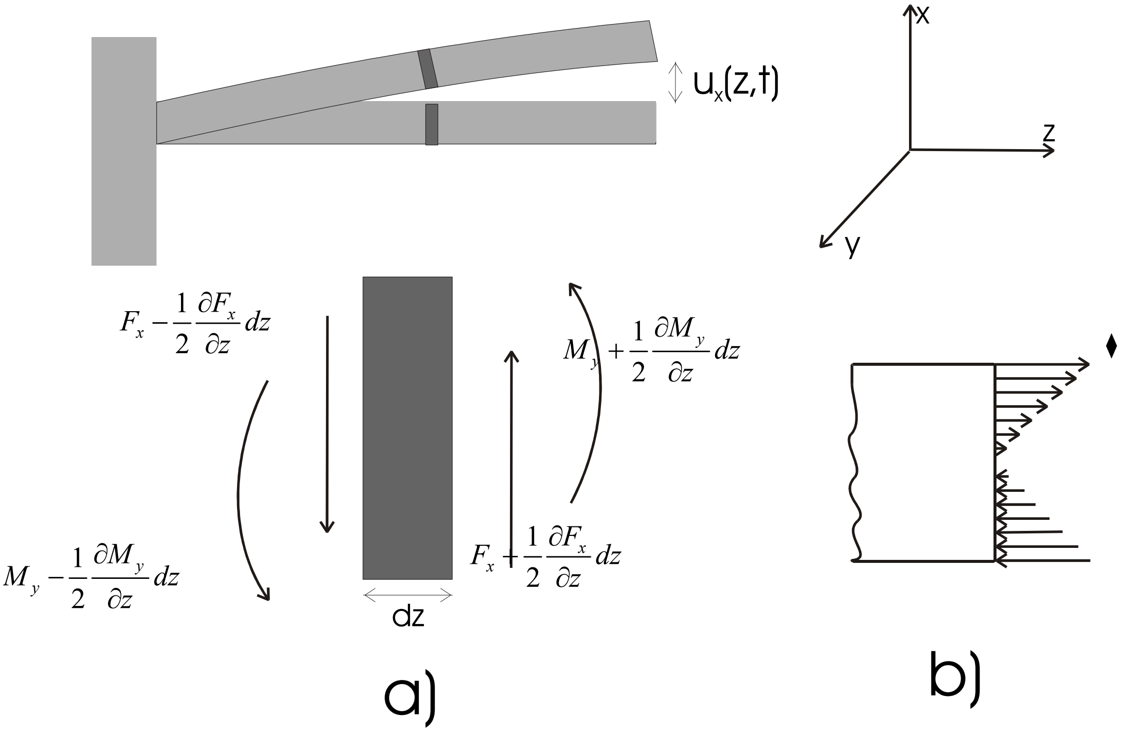

Figure 2.1 Flexural behavior of a straight beam (a) and its stress distribution (b)

2.1.1 Euler-Bernoulli law of elementary beam theory

The problem gets simpler if all shear and rotational forces are negligible (Euler-Bernoulli beam). If not otherwise mentioned, the derivation follows references [22] and [24]. The only remaining normal stress σ_z can be written as

$$\sigma_z = kx \qquad 2.1$$

where k is a constant and x=0 lies in the center of the beam. The total internal force has to be zero and is given by:

$$F_{\text{int}} = \int_A \sigma_z dA = 0 \qquad 2.2$$

With no external momentum applied, the total bending moment is equal to the moment due to internal forces, which are only non vanishing in the y direction (with equation 2.1)

$$M = M_y = \int_A x\sigma_z dA = k\int_A x^2 dA \qquad 2.3$$

The moment of inertia is defined as:

$$I_y = \int_A x^2 dA \qquad 2.4$$

substituting equation 2.4 into 2.3 defines k as:

$$k = \frac{M_y}{I_y} \qquad 2.5$$

The stress of the cross section is therefore given by:

$$\sigma_z = \frac{M_y x}{I_y} \qquad 2.6$$

Using Hook's law the strain (ε) can be calculated

$$\varepsilon_z = \frac{\sigma_z}{E} = \frac{M_y x}{EI_y} \qquad 2.7$$

where E is Young's modulus.

If $u_x(z, t)$ is the displacement of the beam in x direction and the deflection is small ($du_x/dx << 1$), then the second derivative of the deflection is approximately the inverse of the radius of curvature r

$$\frac{\partial^2 u_x(z,t)}{\partial z^2} \approx \frac{1}{r} \qquad 2.8$$

and from figure 2.2 the strain can be found as [25]

$$\varepsilon = \frac{dl - dl_0}{dl_0} = \frac{(r - x)d\theta - rd\theta}{r\sin d\theta} = \frac{-x}{r} \qquad 2.9$$

Combining equations 2.7, 2.8 and 2.9 gives the Euler-Bernoulli law of elementary beam theory:

$$M_y = -EI_y \frac{\partial^2 u_x(z,t)}{\partial z^2} \qquad 2.10$$

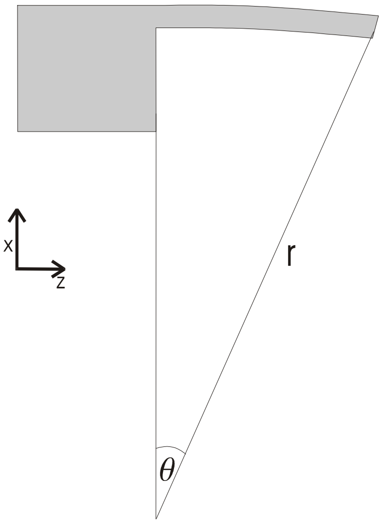

Figure 2.2 Strain in a cantilever

If no external forces or bending moments are acting on the beam the equation of motion is given as

$$m\frac{d^2u_x(z,t)}{dt^2}=\sum F_{\mathrm{int}} \qquad 2.11$$

and the total momentum has to be zero

$$\sum M_{\mathrm{int}}=0 \qquad 2.12$$

the total force can be calculated from figure 2.1

$$\sum F_{\mathrm{int}}=\left(F_x+\frac{1}{2}\frac{\partial F_x}{\partial z}dz\right)-\left(F_x-\frac{1}{2}\frac{\partial F_x}{\partial z}dz\right)=\frac{\partial F_x}{\partial z}dz \qquad 2.13$$

and the sum of the bending moments is

$$\begin{aligned}\sum M_{\mathrm{int}}=&\left(M_y+\frac{1}{2}\frac{\partial M_y}{\partial z}dz\right)-\left(M_y-\frac{1}{2}\frac{\partial M_y}{\partial z}dz\right)\\&+\left(F_x+\frac{1}{2}\frac{\partial F_x}{\partial z}dz\right)\frac{dz}{2}-\left(F_x-\frac{1}{2}\frac{\partial F_x}{\partial z}dz\right)\left(-\frac{dz}{2}\right)\end{aligned} \qquad 2.14$$

Equations 2.14 and 2.12 combined give the relationship between the bending moment and the force

$$F_x = -\frac{\partial M_y}{\partial z} \qquad 2.15$$

With equation 2.15, 2.13 and the mass m=ρAdz (where ρ is the density and A the cross section), the equation of motion (equation 2.11) becomes

$$\rho A \frac{d^2 u_x(z,t)}{d^2 t} = -\frac{\partial^2 M_y}{\partial z^2} \qquad 2.16$$

Now M_y can be replaced in equation 2.16 with 2.10, which leads to the final equation of motion

$$\rho A \frac{d^2 u_x(z,t)}{d^2 t} + EI_y \frac{\partial^4 u_x(z,t)}{\partial z^4} = 0 \qquad 2.17$$

This harmonic linear 4th order differential equation can be solved using separation of variables [22] [24]. In this work we are not concerned with the complete solution, but only the natural resonant frequency of the beam. The natural resonant frequency can be easily obtained by using a Fourier transformation. Applying a Fourier transformation to equation 2.17 with Φ ($u_x(z,t)$)=$U_x(z,\omega)$ leads to

$$\rho A (i\omega)^2 U_x(z,\omega) + EI_y \frac{\partial^4 U_x(z,\omega)}{\partial z^4} = 0 \qquad 2.18$$

The calculation becomes simpler if the equation is rewritten as

$$-\alpha^4 \omega_x{}^2 U_x(z,\omega) + \frac{\partial^4 U_x(z,\omega)}{\partial z^4} = 0 \qquad 2.19$$

with

$$\alpha = \sqrt[4]{\frac{\rho A}{EI_y}} \qquad 2.20$$

The solution of this differential equation is

$$U_x(z,\omega) = A_1 e^{\alpha z\sqrt{\omega}} + A_2 e^{-\alpha z\sqrt{\omega}} + A_3 e^{i\alpha z\sqrt{\omega}} + A_4 e^{-i\alpha z\sqrt{\omega}} \qquad 2.21$$

where A_1, A_2 ,A_3 ,A_4 are complex constants which can be determined by the boundary condition. Using the Euler equations and the comparable equations for sinh and cosh ($\sinh x = \frac{e^x - e^{-x}}{2}$ and $\cosh x = \frac{e^x + e^{-x}}{2}$) equation 2.21 can be transformed to an equation with real constants B_1, B_2, B_3, B_4

$$U_x(z,\omega) = B_1 \sin(\alpha z\sqrt{\omega}) + B_2 \cos(\alpha z\sqrt{\omega}) + B_3 \sinh(\alpha z\sqrt{\omega}) + B_4 \cosh(\alpha z\sqrt{\omega}) \qquad 2.22$$

By applying the boundary conditions of the problem to equation 2.22, the resonant frequency can be found. In the following a cantilever will be considered. Since at the clamped side of the cantilever (z=0) no displacement takes place and the beam is straight, the boundary conditions are given by

$$U_x(0,\omega) = 0 \qquad \frac{dU_x}{dz}(0,\omega) = 0 \qquad 2.23$$

At the free end of the beam (z=L), there is no bending moment and no shear forces that act on the beam

$$\frac{d^2U_x(l,\omega)}{dz^2} = 0 \qquad \frac{dU_x^3(l,\omega)}{dz^3} = 0 \qquad 2.24$$

From the first two boundary conditions, it follows that B_2=B_4 and B_1=-B_3. The last two boundary conditions reduce equation 2.22 to

$$\frac{2 + 2\cos(\alpha l\sqrt{\omega})\cosh(\alpha l\sqrt{\omega})}{\sin(\alpha l\sqrt{\omega}) - \sinh(\alpha l\sqrt{\omega})} = 0 \qquad 2.25$$

A non-trivial solution can be found if

$$\cos(\alpha l\sqrt{\omega})\cosh(\alpha l\sqrt{\omega}) = -1 \qquad 2.26$$

This equation has no analytical solution but can be solved numerical by using the following substitution

$$\beta = \alpha l \sqrt{\omega} \qquad 2.27$$

The values for β_i can be found in table 2.1. From equation 2.20 and 2.19 the natural resonant frequency and its harmonics can be calculated:

$$\omega_i = \frac{\beta_i^{\ 2}}{l^2} \sqrt{\frac{EI_y}{\rho A}} \qquad 2.28$$

The moment of inertia of a beam with circular cross section is given by

$$I_y = \frac{\pi d^4}{64} \qquad 2.29$$

where d is the diameter of the beam and the inertia with a rectangular cross section is

$$I_y = \frac{wt^3}{12} \qquad 2.30$$

For a beam clamped on both sides the boundary conditions are

$$U_x(0,\omega) = 0 \qquad \frac{dU_x}{dz}(0,\omega) = 0 \qquad U_x(L,\omega) = 0 \qquad \frac{dU_x}{dz}(L,\omega) = 0 \qquad 2.31$$

and for a beam free on both sides the boundary conditions are

$$\frac{d^2U_x(0,\omega)}{dz^2} = 0 \qquad \frac{dU_x^{\ 3}(0,\omega)}{dz^3} = 0 \qquad \frac{d^2U_x(l,\omega)}{dz^2} = 0 \qquad \frac{dU_x^{\ 3}(l,\omega)}{dz^3} = 0 \qquad 2.32$$

The solution method is similar to the one for the cantilever. The final solution is the same for the clamped-clamped and the free-free beam and only differs from the cantilever in the factor $\beta_{i,}$, whose values are also listed in table 2.1.

	β^2_i	
i	Cantilever	clamped-clamped and free-free beam
1	3.516	22.373
2	22.034	61.678
3	61.701	120.903
4	120.912	199.860
5	199.855	298.526

Table 2.1 Solution of the equation of motion for a cantilever beam

2.1.2 Damping of an Euler-Bernoulli beam

In the derivation of the resonant frequency damping has been neglected so far. Rast *et al* [26] calculated the resonant frequency and the amplitude response for a cantilever with damping proportional to the displacement (coulomb damping). The damping is introduced by defining a complex Young's Modulus:

$$\hat{E} = E\left(1 + i\frac{1}{Q_{Coulomb}}\right) \tag{2.33}$$

The differential equation for this problem then becomes

$$\rho\frac{\partial^2 u_x(z,t)}{\partial^2 t} + E(1 + i\frac{1}{Q_{Coulomb}})I_y\frac{\partial^4 u_x(z,t)}{\partial z^4} = F(\omega,t) \tag{2.34}$$

For (F(ω,t) =0) he found that for high Q-factor the resonant frequency is approximately the same as for an undamped oscillator. If a time-dependent force is applied to the cantilever, the amplitude response (A_n) can be found as

$$A_n = \frac{|F_0\alpha_n|}{|m|\sqrt{\left(\omega_n^{\ 2} - \omega^2\right)^2 + \left(\frac{\omega_n^{\ 2}}{Q_{Coloumb}}\right)^2}} \tag{2.35}$$

where ω_n is the resonant frequency of the cantilever and α_n is a constant depending on the boundary condition (i.e. the form of the applied force). As seen later, this equation has the same form as the solution of the simple harmonic oscillator. Therefore the cantilever used in this thesis can be approximated with a simple harmonic oscillator.

2.1.3 Timoshenko beam

In the Euler-Bernoulli beam, the shear deformation of the beam was not taken into account. Timoshenko developed a model to overcome that limitation. All other limitations of the Euler-Bernoulli model still apply to the Timoshenko model. Only the main steps are given here, and a more detailed derivation can be found in reference [22].

The shear deformation of the cross section acts in the opposite direction to the deflection of the beam. The cross section is therefore not perpendicular to the (deformed) beam as in the Euler-Bernoulli beam. The rotation can be written as:

$$\phi_y = \frac{\partial u_x}{\partial z} - \gamma_x \tag{2.36}$$

where the shear strain is given by

$$\gamma_x = \frac{\chi F_x}{GA} \tag{2.37}$$

and χ is the shear factor. This shear factor is dependent on the shape of the beam's cross section. G is the rigidity modulus, which is linked to Young's modulus through the Poisson ratio (μ) [27]:

$$G = \frac{E}{2(1+\mu)} \tag{2.38}$$

The bending moment then becomes

$$M_y = EI_y \frac{\partial}{\partial z}\left(\frac{\partial u_x}{\partial z} - \frac{TF_x}{GA}\right) \tag{2.39}$$

Another consequence of taking the rotational inertia of the cross section into account is that the total moment of the beam is no longer equal to zero (as in equation 2.12) but

$$\sum M = \rho I_y dz \frac{\partial^2 \Phi_y}{\partial t^2} \tag{2.40}$$

With the sum of the force and the moment (equation 2.13 and 2.14) the two governing equations become

$$\begin{aligned} m\frac{\partial^2 u_x(z,t)}{\partial^2 t} &= \frac{\partial F_x}{\partial z} \\ \rho I_y \frac{\partial^2 \Phi_y}{\partial t^2} &= F_x + \frac{\partial M_y}{\partial z} \end{aligned} \tag{2.41}$$

With equation 2.36 and 2.37 equation 2.41 can be combined and solved for F$_x$

$$\rho I_y \frac{\partial^4 u_x}{\partial z^2 \partial t^2} - \frac{\rho^2 I_y \chi}{G}\frac{\partial^4 u_x}{\partial t^4} - \rho A \frac{\partial^2 u_x}{\partial t^2} - EI_y \frac{\partial^4 u_x}{\partial z^4} + \frac{EI_y \rho \chi}{G}\frac{\partial^4 u_x}{\partial z^2 \partial t^2} = 0 \tag{2.42}$$

This differential equation was first solved by Goen in 1931 [28]. Pickett [29] gives a good summary of Goen's work and includes some application notes. Due to the length of the solution for an actual thin beam, it is not included and only an advancement of this solution is given in the next paragraph.

2.1.4 Empirical approaches for a cantilever

The Timoshenko beam is still an approximation and the solution found by Goen does not fulfill all boundary conditions [29]. Since it is very difficult to find a model that implements all material and geometric characteristics an empirical model is necessary. This empirical relationship was determined by the American Society for Testing and Materials (ASTM) [30] based on Goen's and Pickett's work. For a free-free beam with rectangular cross section the resonant frequency can be found as

$$f_f = 1.028 \frac{t}{l^2} \frac{1}{\sqrt{T(t,l)}} \sqrt{\frac{E}{\rho}} \tag{2.43}$$

		Resonant frequency [MHz]		Relative error	Correction factor T
		Euler-Bernoulli	ASTM		
t=200 nm	l =1μm	1649.7	1469.6	0.12	1.260
	l =4μm	103.1	102.2	0.008	1.017
	l =8μm	25.8	25.7	0.002	1.004
t=350 nm	l =1μm	2886.8	2183.6	0.322	1.748
	l =4μm	180.4	175.9	0.026	1.052
	l =8μm	45.1	44.8	0.006	1.013

Table 2.2 Comparison of an Euler-Bernoulli beam with the analytical solution for a free-free rectangular beam

The equation differs from the resonant equation derived for an Euler-Bernoulli Beam only by a correction factor T(t,l).

$$\begin{aligned}T(t,l) = {} & 1.000 + 6.585(1.000 + 0.075\mu + 0.811\mu^2)\left(\frac{t}{l}\right)^2 - 0.868\left(\frac{t}{l}\right)^4 \\ & - \left[\frac{8.340(1.000 + 0.202\mu + 2.173\mu^2)\left(\frac{t}{l}\right)^4}{1.000 + 6.338(1 + 0.141\mu + 1.537\mu^2)\left(\frac{t}{l}\right)^2}\right]\end{aligned} \tag{2.44}$$

It can be seen that for t << l the correction factor T becomes equal to 1. The correction factor for an Euler-Bernoulli beam with a circular cross-section is given as

$$\begin{aligned}T(d,l) = {} & 1.000 + 4.939(1.000 + 0.075\mu + 0.811\mu^2)\left(\frac{d}{l}\right)^2 - 0.4883\left(\frac{d}{l}\right)^4 \\ & - \left[\frac{4.691(1.000 + 0.202\mu + 2.173\mu^2)\left(\frac{d}{l}\right)^4}{1.000 + 4.754(1.000 + 0.141\mu + 1.537\mu^2)\left(\frac{d}{l}\right)^2}\right]\end{aligned} \tag{2.45}$$

The experiments done by the ASTM to obtain the correction factor were done on a large scale beam at low frequencies. Therefore it should be kept in mind that the correction factors might have some errors if applied to high frequency NEMS and MEMS. The ASTM standard assumes a homogeneous material. Due to the high surface to volume ratio it is questionable whether an NEMS device could be assumed to be homogeneous. Table 3.2 shows the error that is introduced by the Euler-Bernoulli approximation, which is only significant for short beams.

2.2 Classical Harmonic Oscillation

As it can be seen from the complexity of the derivation of the resonant frequency it will be difficult to model the behavior of these devices using continuous mechanics. It would be desirable to describe the resonator using a system with one-degree of freedom. The simplest one-degree of freedom system is a massless spring with a spring constant k and a mass m attached to the spring. This oscillator will be discussed in detail here and we will show that by adjusting the spring constant and the mass it can describe the vibration of more complex structures like a cantilever or even paddle resonators. Neglecting damping, the equation of motion of a harmonic oscillator is given as

$$m\frac{d^2}{dt^2}x(t)+kx(t)=0 \tag{2.46}$$

The solution of this equation is

$$x(t)=A_1\sin(\sqrt{\tfrac{k}{m}}t)+A_2\cos(\sqrt{\tfrac{k}{m}}t) \tag{2.47}$$

Which leads to a resonant frequency of

$$\omega_0=\sqrt{\frac{k}{m}} \tag{2.48}$$

Comparing this equation with equation 2.43 shows that a beam resonator can be approximated with a simple harmonic oscillator if an effective spring constant k_{eff} and an effective mass m_{eff} is defined [31].

$$m_{eff} = \rho A l \tag{2.49}$$

$$k_{eff} = \frac{\beta_i^4}{T(t,l)} \frac{EI_y}{l^3} \tag{2.50}$$

where β_i depends on the mode and can be found in table 2.1. The damping can be included in equation 2.46 by defining a complex spring constant for damping proportional to the displacement (i.e. coloumb damping) [25]

$$\hat{k} = k\left(1 + i\frac{1}{Q_{Coulomb}}\right) \tag{2.51}$$

By adding a frictional force that is proportional to the velocity (viscous damping) [32].

$$F_{friction} = \gamma \dot{x}(t) = \frac{m\omega_0}{Q_{viscous}} \dot{x}(t) \tag{2.52}$$

The equation of motion with a periodical driving force is then

$$\ddot{x}(t) + \frac{\omega_0}{Q_{viscous}} \dot{x}(t) + \omega_0^2 (1 + i\frac{1}{Q_{Coulomb}}) x(t) = \frac{F_0}{m} e^{i\omega t} \tag{2.53}$$

The solution of this equation must have the following form

$$x(t) = A_1 e^{i\omega t} + A_2 e^{-i\omega t} \tag{2.54}$$

To find the factors A_1 and A_2 equation 2.54 can be inserted into equation 2.53

$$\begin{aligned} &A_1\left(\omega_0^2 \text{-} \omega_f^2 + \mathrm{i}\left(\frac{\omega_0}{Q_{coloumb}} - \frac{\omega_0 \omega_f}{Q_{viscous}}\right)\right) e^{i\omega_f t} + \\ &A_2\left(\omega_0^2 \text{-} \omega_f^2 + \mathrm{i}\left(\frac{\omega_0}{Q_{coloumb}} + \frac{\omega_0 \omega_f}{Q_{viscous}}\right)\right) e^{-i\omega_f t} = \frac{F_0}{m} e^{i\omega_f t} \end{aligned} \tag{2.55}$$

It follows that $A_2=0$ and the solution for x(t) is therefore

$$x(t)=\frac{F_0}{m}\left(\frac{Q_{coloumb}}{Q_{viscous}}\omega_0^2\omega_{\mathrm{f}}^2-\omega_0^3\omega_{\mathrm{f}}+\frac{Q_{viscous}}{Q_{coloumb}}\omega_0^4+Q_{viscous}Q_{coloumb}\left(\omega_{\mathrm{f}}^2-\omega_0^2\right)^2\right)^{-1} \\ \left[Q_{viscous}Q_{coloumb}\left(\omega_0^2-\omega_{\mathrm{f}}^2\right)+i\left(Q_{coloumb}\omega_0\omega_{\mathrm{f}}-Q_{viscous}\omega_0^2\right)\right]e^{i\omega_{\mathrm{f}}t} \qquad 2.56$$

which can be rewritten as

$$x(t)=\frac{F_0}{m}\left(\left(\frac{\omega_0\omega_{\mathrm{f}}}{Q_{viscous}}-\frac{\omega_0^2}{Q_{coloumb}}\right)^2+\left(\omega_{\mathrm{f}}^2-\omega_0^2\right)^2\right)^{-1/2}e^{i(\omega t+\psi)} \qquad 2.57$$

where ψ is the phase difference

$$\psi=\tan^{-1}\left(\frac{\omega_0\omega_{\mathrm{f}}}{Q_{viscous}\left(\omega_0^2-\omega_{\mathrm{f}}^2\right)}-\frac{\omega_0^2}{Q_{coloumb}\left(\omega_0^2-\omega_{\mathrm{f}}^2\right)}\right) \qquad 2.58$$

The actual amplitude of the vibration is then given by

$$A(\omega_{\mathrm{f}})=\frac{F_0}{m}\frac{1}{\sqrt{(\omega_0^2-\omega_{\mathrm{f}}^2)^2+\left(\frac{\omega_0^2}{Q_{coloumb}}+\frac{\omega_0\omega_{\mathrm{f}}}{Q_{viscous}}\right)^2}} \qquad 2.59$$

For $Q_{viscous}=0$ equation 2.59 is similar to the amplitude response calculated by Rast *et al* (equation 2.35) [26]. Since it only differs by a proportionality factor that depends on the form of the applied force and the boundary condition, beam resonators can be approximated with a simple harmonic oscillator. Equation 2.59 shows that the frequency where the amplitude is maximum is not at the resonant frequency ω_0 but is actually quality factor dependent. Since finding the resonant frequency is straightforward but tedious, only the case where $Q_{cloumb}=0$ will be considered here, which is

$$\omega_{\max}=\omega_0\sqrt{\left(1-\frac{1}{2Q_{viscous}^2}\right)} \qquad 2.60$$

In the limit of a high quality factor (Q) the amplitude will only be significant for the region where $\omega_f \approx \omega_0$, therefore $\omega_f\omega_0 \approx \omega_0^2$ and $\omega_f + \omega_0 \approx 2\omega_0$. With this substitution equation 2.59 becomes

$$A(\omega_\mathrm{f}) = \frac{F_0}{k}\frac{1}{\sqrt{4\left(\frac{\omega_0-\omega_\mathrm{f}}{\omega_0}\right)^2+\left(\frac{1}{Q_{coloumb}}+\frac{1}{Q_{viscous}}\right)^2}} \qquad 2.61$$

In the limit of large Q we than find that

$$\frac{1}{Q_{tot}} = \frac{1}{Q_{coloumb}}+\frac{1}{Q_{viscous}} \qquad 2.62$$

and equation 2.61 becomes

$$A_{\max}(\omega_\mathrm{f}) = \frac{F_0}{k}\frac{1}{\sqrt{4\left(\frac{\omega_0-\omega_\mathrm{f}}{\omega_0}\right)^2+\left(\frac{1}{Q_{tot}}\right)^2}} \qquad 2.63$$

Equation 2.63 has the form of a Lorentzian. The experimental data can be fitted to that equation to obtain the Q factor and the resonant frequency. But from equation 2.63 a quicker way to calculate Q_{tot} can be derived. The maximum amplitude at resonance is given by

$$A_{\max} = \left|\frac{F_0}{k}\right| Q_{tot} \qquad 2.64$$

The amplitude is reduced to half its original value if

$$\frac{1}{2}Q_{tot} = \frac{1}{\sqrt{4\left(\frac{\omega_0-\omega_{half}}{\omega_0}\right)^2+\left(\frac{1}{Q_{tot}}\right)^2}} \qquad 2.65$$

or

$$\sqrt{\frac{3}{4}}\frac{1}{Q_{tot}} = \frac{\omega_0-\omega_{half}}{\omega_0} \qquad 2.66$$

The half bandwidth Δω is the peak width at half the amplitude and therefore

$$\Delta\omega = 2(\omega_0 - \omega_{half}) \tag{2.67}$$

and the quality factor is given as

$$Q_{tot} = \sqrt{3}\frac{\omega_0}{\omega_{halfbandwith}} = 1.73\frac{f_0}{f_{halfbandwith}} \tag{2.68}$$

This expression will be used later to calculate the Q factor from the data obtained in the experiments.

2.3 Application to nanomechanical paddles

Paddle resonators are a better choice for sensor applications where high frequencies are not necessary. The surface of a paddle is larger than the surface of a cantilever or a double clamped beam, therefore their active sensing area is larger. The larger surface is also interesting from a research point of view, as it allows the investigation of interestinmg surface-related phenomena. In addition, the deflection also will be much larger compared with the one of cantilevers or beams, which makes it easier to detect their vibration. Hence paddle resonators have been chosen for these experimental studies. It can be seen in figure 2.4b, that paddles resonate in two different modes, a torsional and a translational mode. In the following, the two modes are discussed separately.

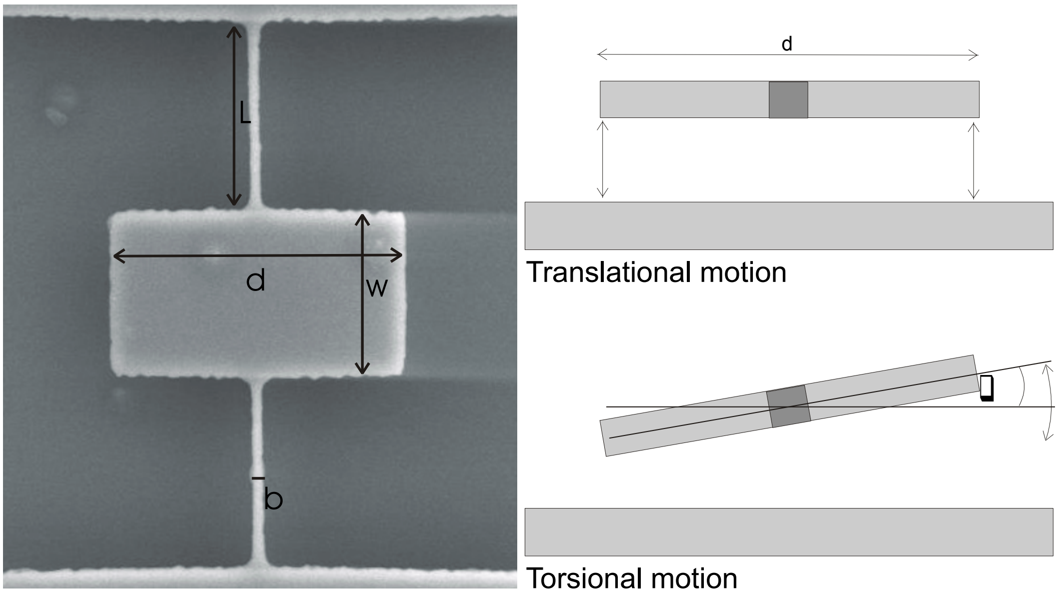

a) b)

Figure 2.3 Geometry of a paddle (the thickness of the paddle is a and the gap between substrate and the resonator is h) (a) and the modes of its motion (b)

2.3.1 Translational motion

Olkhovets model

In the simplest model, it can be assumed that the paddle stays undeformed during the motion due to its relatively high rigidity [34] [35]. Therefore each support beam can be considered as a beam clamped on both sides. From symmetry considerations, it follows that the point in the middle of each beam will not bend and is consequently under no flexural tension. The beam is therefore regarded as two half-length beams clamped at their opposite ends with a joining point in the middle. It is also assumed that the deflection is symmetric so that the deflection from each half-length beam is half of the total deflection.

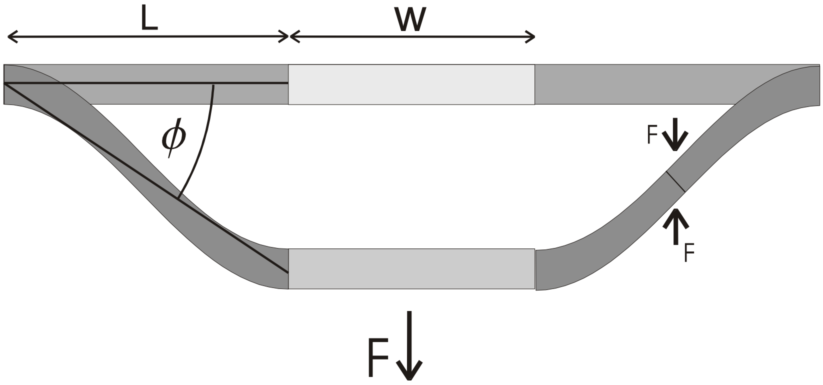

Figure 2.4 Olkhovets model for the translation mode of the paddle

Experimentally a nonlinear resonant peak was observed. To take that behavior into account a non-linear restoring force was introduced. The equation of motion is then

$$\ddot{x} + 2\frac{Ea^3b}{ML^3}x + \frac{1}{2}\frac{Eab}{ML^3}x^3 + \frac{1}{\omega_0 Q}\dot{x} = F_0 e^{-i\omega t} \qquad 2.69$$

Negelecting the damping, for small amplitudes the resonace frequency of the paddle can be found as

$$f_0 = 0.22\sqrt{\frac{Ea^3b}{ML^3}} \qquad 2.70$$

This model does not take shear deformation into account. This can be introduced by the correction factor T(t,l) (equation 2.44) with t=a and l=L/2 and the resonant frequency is then

$$f_0 = 0.22\sqrt{\frac{1}{T(a,\frac{L}{2})}\frac{Ea^3b}{ML^3}} \qquad 2.71$$

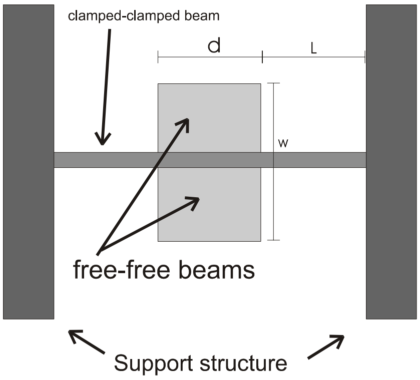

Figure 2.5 Dowell model of a paddle

Dowell model

Since the assumption that the paddle does not bend is very crude, Dowell introduced an advanced model [36] that better predicts the resonant frequency. In his approach the paddle resonator is divided into a long clamped-clamped beam and into two free-free beams attached to it at the side as shown in figure 2.6 [36].

If all bending in the y direction is neglected, one-dimensional Lagrange's equations can be used to find the resonant frequency. The kinetic and potential energy of a clamped-clamped beam and free-free beam were defined separately. We then require that the displacement at the joint of the two parts be the same. If only the fundamental mode of motion is considered in the calculation of the kinetic energy (single mode) of the resonator, the resonant frequency can be found as

$$f_0 = 0.14\sqrt{\frac{a^3 b}{L^3 adw}\frac{E}{\rho}} \qquad 2.72$$

Further improvements of the model can be achieved if the energy of the harmonic modes is included in the kinetic energy (multi mode). Then the resonant frequency changes to

$$f_0 = 0.19\sqrt{\frac{a^3 b}{L^3 adw}\frac{E}{\rho}} \qquad 2.73$$

With regards to the following numerical simulation it is important to remark that for the derivation of the resonant frequency a Poisson's ratio of 0.3 is used, but the Poisson ratio has little influence on the actual results.

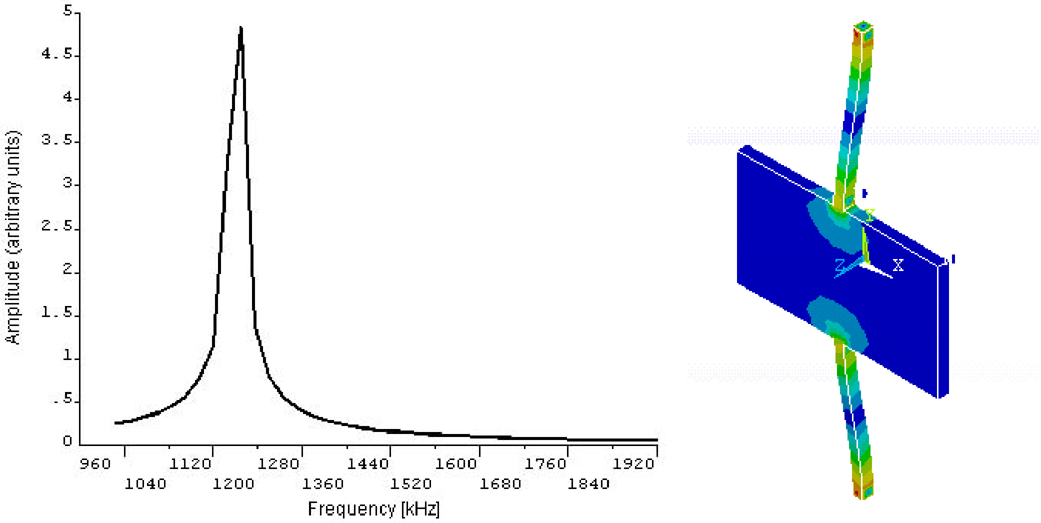

a) b)

Figure 2.6 Results of the FEM simulation of the translational mode, resonant frequency (a) and stress distribution (b)

Numerical simulation

Both previously described models predict a different resonant frequency and both idealize the behavior of the paddle. A more precise prediction of the behavior of the paddles should be possible with finite element modeling (FEM). In collaboration with Christopher Maxey, the frequency response of the motion of a paddle was modeled using the software package ANSYS [37]. The size of the simulated paddle was similar to the one used in the experiment with a=200nm, b=175nm, L=2.5 µm, w=2 µm, d=3.5µm. Young's modulus for silicon used in this simulation was E=150 GPa and a Poisson ratio of .17 and a density of 2330 kg m^{-3}. The force per unit on the paddle was assumed to be 200N m^{-2}, which yields a total force on the paddle of approximately 1.5 nN. The resonant frequency was found to be 12.4 MHz and it can be seen from figure 2.7 that the paddle does not stay undeformed as assumed in the Olkhovets model.

In the FEM simulation an additional resonance mode was found with a resonant frequency at 129.2 MHz (figure 2.7). The motion of this mode looks like the flap of a butterfly. We were not able to measure that mode. A reason for this is that since the frequency is ten times larger than for the translational mode, the spring constant for this

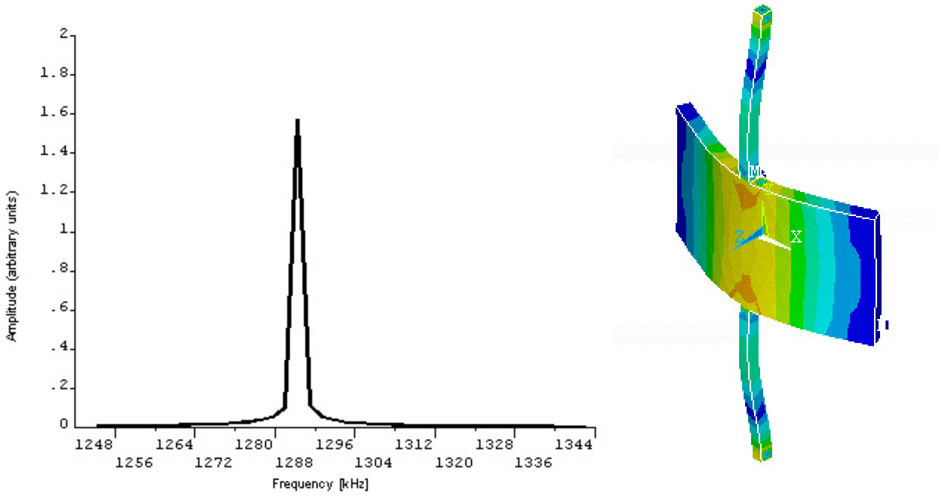

a) b)

Figure 2.7 Results of the FEM simulation of the butterfly mode, resonant frequency (a) and stress distribution (b)

mode is 100 times larger; therefore also 100 times the force is needed to excite that mode. But this mode has probably less clamping losses than the translational mode, because it can be considered as free-free beam [38].

Conclusion

For comparison of the two models with the FEM simulation the resonant frequency of the simulated paddle is calculated. The results are listed in table 2.3. The Olkhovets model estimates the resonant frequency too high, because the whole paddle is not rigid. Introducing the correction factor into Olkhovets model estimates the resonant frequency better, but due to the deformation of the paddle it is still estimated too high. The multi mode model of Dowell estimates the resonant frequency fairly well.

	Resonant of translational mode	
	Equation	Numerical [MHz]
Olkhovets model	$f_0 = 0.22\sqrt{\frac{a^2b}{L^3dw}\frac{E}{\rho}}$	14.5
Corrected Olkhovets model	$f_0 = 0.22\sqrt{T(a,\frac{L}{2})\frac{Ea^3b}{ML^3}}$	13.4
Dowell model (single mode)	$f_0 = 0.14\sqrt{\frac{a^2b}{L^3dw}\frac{E}{\rho}}$	9.3
Dowell model (multi mode)	$f_0 = 0.19\sqrt{\frac{a^2b}{L^3dw}\frac{E}{\rho}}$	12.1
ANSYS Simulation	FEM-model	12.4 (12.3 with Poisson ratio of 0.3)

Table 2.3 Comparison of different models for a paddle oscillator

2.3.2 Torsional motion

Micromechanical torsional oscillators have been used to detect very small strains. This makes them ideal for studies of magnetism [39]. For a better understanding of this mode a model will be developed in this paragraph.
Assuming the support beams are massless, the torsional motion of a paddle can be described with the following differential equation [24]

$$I_{paddle}\ddot{\theta}(t) + \frac{2\sqrt{I_{paddle}\kappa_{beam}}}{Q_{system}}\dot{\theta}(t) + 2\kappa_{beam}\theta(t) = \tau(\theta,t) \qquad 2.74$$

By dividing this equation by two and neglecting damping it becomes the equation for a simple torsional oscillator.

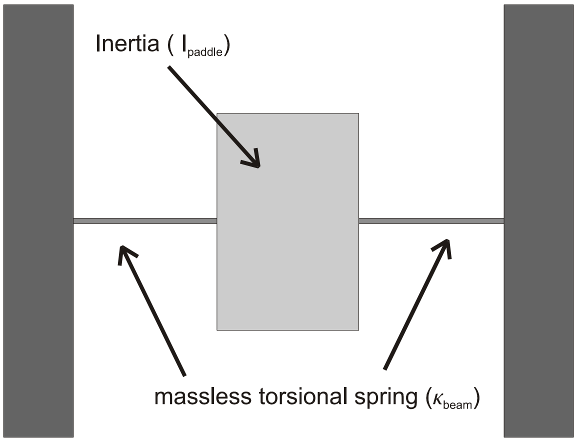

Figure 2.8 Torsional model of paddle

Therefore the paddle can also be considered as a single clamped beam with an inertial mass $I_{Paddle}/2$ attached to its end. The governing equation of the torsional vibration of the shaft is given as [24]

$$\frac{\partial^2\theta(x,t)}{\partial t^2}=\frac{G}{\rho}\frac{\partial^2\theta(x,t)}{\partial x^2} \tag{2.75}$$

The solution for this equation can be found using separation of variables

$$\theta(x,t)=\left(A_1\sin\left(\omega x\sqrt{\frac{\rho}{G}}\right)+A_2\cos\left(\omega x\sqrt{\frac{\rho}{G}}\right)\right)\left(B_1\sin(\omega t)+B_2\cos(\omega t)\right) \tag{2.76}$$

where A_1, A_2, B_1, B_2 and ω are constants.

The system does not experience any displacement for x=0 which leads to the first boundary condition:

$$\theta(0,t)=0 \tag{2.77}$$

At the end of the beam (x=L) the internal torque of the beam has to be the same as the external torque from the “half” paddle:

$$GI_{beam}\frac{\partial\theta(x,t)}{\partial x}=-\frac{I_{Paddle}}{2}\frac{\partial^2\theta(x,t)}{\partial t} \tag{2.78}$$

The first boundary condition leads directly to A_2=0 and the second one to

$$\frac{\omega L}{c}\tan\frac{\omega L}{c}=\frac{2\rho L I_{beam}}{I_{Paddle}} \tag{2.79}$$

This equation has no analytical solution but can be solved numerical with the following substitution

$$\beta=\frac{\omega L}{c} \tag{2.80}$$

Unlike for translational motion, it is not possible to find a general factor β that suits all systems. Equation 2.79 has to be solved numerical for each system.

Other authors [34] [35] approximated the support beams of the paddle as simple beam and found the following resonant frequency

$$f_0=\frac{1}{2\pi}\sqrt{2\beta\left(\frac{a}{b}\right)\frac{ab^3}{L\,I_{paddle}}G} \tag{2.81}$$

where β(a/b) is a dimensionless function of the ratio a/b, with β(1.14)=0.16.
The moment of inertia for a symmetric paddle and a rectangular beam are given as [40]

$$\begin{aligned} I_{Paddle} &= \frac{d^2}{2}\rho dwa \\ I_{beam} &= \frac{a^2+b^2}{12}\rho abL \end{aligned} \tag{2.82}$$

	Resonant Frequency		
	Equation	Symmetric	50 nm asymmetric
Beam with intertial mass	$\omega L\sqrt{\frac{\rho}{G}}\tan\left(\omega L\sqrt{\frac{\rho}{G}}\right)=\frac{2\rho LI}{I_{Pad}}$	2.86 MHz	2.82 MHz
Simple beam	$f_0=0.09\sqrt{\frac{ab^3}{L\ \ I_{paddle}}G}$	3.34 MHz	3.28 MHz

Table 2.4 Comparison of the torsional resonant frequency of two different models with an FEM simulation

The predicted frequency of the two models differs only by 17 % and should give an upper and lower limit of the actual resonant frequency, since the resonant frequency predicted by the model of Dowell [36] lays in between the two models given in the table 2.4.

Since a uniform area force will be applied over the whole paddle, it will not resonate in the torsional mode if it is perfectly symmetric. But small asymmetries are randomly introduced during the fabrication process of these devices. To model this asymmetry a shift ($d_{asym}/2$) of the vibration axis from the center to one side can be assumed. One side of the paddle is than d_{asym} larger than the other one. The new inertia of the paddle can be calculated using Steiner's theorem [40].

$$I_{asym\ Paddle}=I_{Paddle}+\left(\frac{d_{asym}}{2}\right)^2\rho dwa \qquad 2.83$$

This asymmetry introduces a resulting torque (equation 2.84) that acts on the paddle and sets the paddle in motion.

$$\tau(\theta,t)=F_{unit}(V,t)wd_{asym}\left(\frac{d}{2}-\frac{d_{asym}}{2}\right)\cos\theta \qquad 2.84$$

After the paddle is set in motion the gap dependency (h) of the force introduces an additional torque and can be found as [35]

$$\tau(\theta,t) \approx F_{unit}(V,t)\frac{wd^3}{12h}\theta \qquad 2.85$$

Which leads to the following equation of motion

$$I\ddot{\theta} + \kappa\theta + \frac{I}{\omega_0 Q}\dot{\theta} = F_{unit}(V,t)wd\left(V_{DC}^2 + 2V_{DC}V_{AC}\cos(\omega t) + V_{AC}^2\cos^2(\omega t)\right)$$
$$\left(\frac{d_{asym}}{d}\left(\frac{d}{2} + \frac{d_{asym}}{4}\right)\cos\theta + \frac{d^2}{6h}\theta\right) \qquad 2.86$$

With d >> d_{asym} and an expansion for the cosines the equation can be rewritten as

$$I\ddot{\theta} + \kappa\theta + \frac{I}{\omega_0 Q}\dot{\theta} = F_{unit}(V,t)wd\left(V_{DC}^2 + 2V_{DC}V_{AC}\cos(\omega t)\right)\left(\frac{d_{asym}}{2}\left(1 - \frac{\theta^2}{2}\right) + \frac{d^2}{6h}\theta\right) \qquad 2.87$$

All higher order terms of the cosines expansion were neglected, as well as the $V^2_{AC}\cos^2(\omega t)$ term. Further the damping and, since the deflection is small, nonlinear terms were neglected, which reduces equation 2.87 to

$$I\ddot{\theta} + \left(\kappa - \left(F_{unit}(V,t)wd\right)V_{DC}^2\frac{d^2}{6h}\right)\theta = \frac{d_{asym}}{2}\left(F_{unit}(V,t)wd\right)V_{DC}^2 \qquad 2.88$$

Which leads finally to a DC potential dependence of the resonant frequency

$$f = f_0\sqrt{1 - \frac{\left(F_{unit}(V,t)wd\right)d^2}{6\kappa h}V_{DC}^2} \qquad 2.89$$

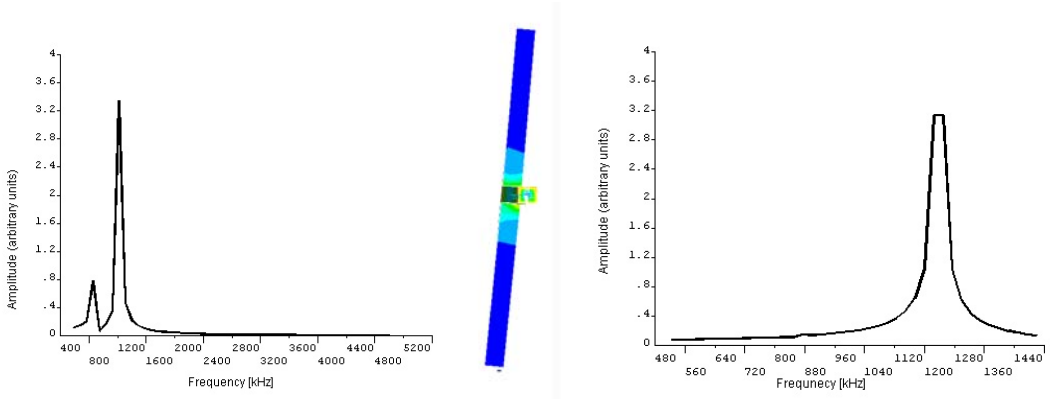

a) b) c)

Figure 2.9 Results of the FEM simulation with an asymmetry of 50 nm, resonant frequency (a) and stress distribution (top view) (b) and with an asymmetry of 10 nm (c)

Numerical simulation

An FEM simulation was done for a paddle with an asymmetry of 50 nm. Beside the peak for the translational motion, a smaller peak around 9 MHz was found. As seen in figure 3.12 it can be identified as a superposition of a torsional and a translational mode. The paddle was not resonating with the center at rest, but with the edges of the shorter sides at rest. The paddles used in this work were intended to be symmetric, but an asymmetry was introduced randomly in the fabrication process. Thus the simulation was done again with an asymmetry of 10 nm. As seen in figure 2.11 the small asymmetry results in no additional resonant peak, but the peak itself has a plateau. The shape of motion at different frequencies on the plateau changes continuously from the torsional to the translational modes, i.e. a sideward motion occurred. The vicinity of the different modes will make it difficult to always obtain the same mode during the experiment.

3 Loss mechanisms

For many applications resonators with high quality factor are needed. For filter applications in wireless systems, it may be necessary to filter out a weak signal in the vicinity of a strong interfering signal. Since the output signal of a filter is proportional to the amplitude of the resonator, the signal of interest may still be superposed with the interfering signal of the same magnitude if a resonator with a low quality factor is used. High quality factors are therefore needed to reduce the interfering signal. For sensor applications, the shift of the resonance frequency can be determined more precisely if the resonator has a higher quality factor, leading to greater sensitivity. No NEMS resonator with a higher quality factor than 10^7 have been reported [17]; most NEMS do not even come close to this value. In macroscopic resonators much higher Q-factors can be obtained. Therefore the origin of losses in NEM resonators must be understood in order to increase the quality factor.

The loss mechanisms described in part 3.2 (air damping) and 3.3 (clamping losses) are extrinsic loss mechanisms: they have nothing to do with the material itself but are influenced by the design of the structure. The loss mechanisms discussed in paragraph 3.4 to 3.6 are intrinsic loss mechanisms that will limit the highest possible achievable Q-factor. Paragraph 3.7 discusses surface related loss mechanisms. In addition loss mechanism associated with stress relaxation will be discussed in the next chapter.

Most of the theoretical and experimental work on energy dissipation was done with large oscillators at low frequencies (~1 Hz), which makes it questionable whether the theoretical description of the loss mechanism can be easily applied to high frequency NEMS.

3.1 Energy dissipation and quality factor

The extent of the energy dissipation is often expressed in the form of a quality factor [41]. The quality factor Q is defined as

$$\frac{1}{Q}=\frac{1}{2\pi}\frac{\text{Energy loss per cycle}}{\text{Total elastic energy}} \tag{3.1}$$

This can easily be seen for an oscillator with coulomb damping ($\hat{E}=E(1+i\eta)$). Assuming the applied external stress has the following form

$$\sigma=\sigma_0 e^{i\omega t} \tag{3.2}$$

The strain response will then have a phase shift

$$\varepsilon=\varepsilon_0 e^{i\omega t+\phi} \tag{3.3}$$

due to the complex part of the modulus. The elastic energy stored in the oscillator is

$$W=\frac{1}{2}E\sigma_0^2 \tag{3.4}$$

The energy that is dissipated per cycle is

$$\Delta W=\pi E\eta\sigma_0^2 \tag{3.5}$$

which then gives us

$$\frac{1}{Q}=\frac{\Delta W}{2\pi W}=\tan\phi=\eta \tag{3.6}$$

The energy dissipation can also be expressed in the form of a complex resonant frequency [42]. The real part gives the resonant frequency and the imaginary part the damping. The mechanical energy is proportional to the square of its amplitude, the inverse of the quality factor can therefore be written as

$$\frac{1}{Q}=2\left|\frac{\operatorname{Im}(\omega)}{\operatorname{Re}(\omega)}\right| \tag{3.7}$$

In general, different energy dissipation mechanisms contribute to the quality factor. An individual quality factor can be assigned to the different mechanisms. The overall Q-factor of a system can then be found as the sum of the inverses of the individual Q-factors

$$\frac{1}{Q_{tot}}=\sum\frac{1}{Q_i} \qquad 3.8$$

3.2 Air friction

Air damping can be separated into an intrinsic, a molecular, and a viscous region. In the intrinsic region, air friction is not a significant source of energy loss. In general, the interaction of the surroundings with the beam can be summarized with a drag force F_{drag} [43]. The drag force has the following form

$$F_{drag}=\left(\beta_1+i\beta_2\right)\dot{u}_x=\beta_1\dot{u}_x-\frac{\beta_2}{\omega}\dot{u}_x=\gamma_1 L\dot{u}_x-\frac{\gamma_2 L}{\omega}\dot{u}_x \qquad 3.9$$

where $\dot{u}_x$ is the velocity and L the length of the beam. It can be shown that γ_1 is proportional to the quality factor and γ_2 is proportional to the frequency shift.

3.2.1 Viscous region

For higher pressure, in the viscous region the gas acts as a viscous fluid [43]. Assuming that the air is incompressible and that the Reynolds number is small (no turbulences) the force on the surface can be calculated using the Navier-Stokes and the continuity equation. The beam will be approximated with a row of spheres vibrating independently of each other, because it is difficult to determine the velocity field of the air around the vibrating beam. The force on the surface is then given as

$$F_{drag}=\left[6\pi\mu r\left(1+\frac{r}{\delta}\right)-i\frac{2}{3}\pi r^3\rho_{gas}\left(1+\frac{9}{2}\frac{\delta}{r}\right)\omega\right]v \qquad 3.10$$

where μ the dynamic viscosity of the medium and ρ_0 the density of the gas, which for an ideal gas is:

$$\rho_0 = \frac{M}{RT} p \qquad 3.11$$

δ is the region around the beam where the motion of the gas is turbulent and is approximately:

$$\delta = \left(\frac{2\mu}{\rho_0 \omega} \right)^{1/2} \qquad 3.12$$

From the drag force it is easy to obtain the Q-factor and the frequency shift.

$$Q = \frac{\rho_{beam} A}{\gamma_1} \omega_0 = \frac{\rho_{beam} wtl}{6\pi\mu r \left(1 + \frac{r}{\gamma}\right)} \omega_0 \qquad 3.13$$

$$\frac{\Delta\omega}{\omega_0} = -\frac{1}{2} \frac{\gamma_2}{\rho_{beam} A} = -\frac{\pi r^3 \rho_0}{3\rho_{beam} lwt} \left(1 + \frac{9}{2} \frac{\delta}{r}\right) \qquad 3.14$$

For the calculation, the radius r can be approximated with the width of the beam.

3.2.2 Molecular region

At low pressure the collisions of the air molecules with the resonator surface can be considered independent of each other [43]. The force on the resonator is due to these collisions. The damping parameter γ_1 is proportional to the air pressure p and the width of the beam w

$$\begin{aligned} \gamma_1 &= \left(\frac{32M}{9\pi RT} \right)^{½} wp \\ \gamma_2 &= 0 \end{aligned} \qquad 3.15$$

where R is the gas constant and M the mass of the gas molecules ($M_{air} \approx 29$ g/mol). The quality factor is then simply

$$Q = \frac{\rho_{beam} A \omega_0}{\gamma} = \left(\frac{9\pi RT}{32M} \right)^{1/2} \frac{t \rho_{beam} \omega_0}{p} \qquad 3.16$$

where ρ is the density of the beam material.

Blom *et al* [43] found the transition from the viscous to the molecular regime around one torr and from molecular to the intrinsic regime between 10^{-2} and 10^{-3} torr for a cantilever with a cross section in the mm^2 range.

3.2.3 Squeeze force

If the gap (h_0) between the beam and the supporting surface is small a squeeze force acts between the beam and the surface [44]. This force can be calculated using the Reynholds equation. The Q-factor can be found as

$$Q = \frac{\rho_{beam} h_0^3 t}{\mu w^2} \omega_0 \qquad 3.17$$

This approximation holds if the beam is much longer than it is wide, and if the initial gap is uniform and the vibration is much smaller than the gap.

It is assumed that the pressure is constant around the resonator, which might not be true, since the pumping effect resulting from the vibration might introduce an inhomogeneous pressure distribution underneath the resonator [45]. In an experimental setup, we therefore must consider that the small size of the gap between the resonator and the substrate reduces the effective pumping speed underneath the resonator. The pressure underneath the resonator is therefore probably higher than on the top of the resonator.

3.3 Clamping

Since real elements are never perfectly rigid, energy can be dissipated from the resonator to the support structure, where local deformations and microslip can occur. The rhodium structures of chapter seven can be considered as a beam fixed at one end by a rigid clamp. At the contact area between the beam and the clamp, slip occurs if the beam bends. The energy loss per cycle is proportional to the inverse of the friction force at the contact area. Increasing the pressure on the beam therefore reduces the energy losses [46]. It is often not possible to increase the rigidity of the support, but energy losses can be reduced with an optimized design. Olkhovets [43] showed that a double beam with a flexible support improves the Q factor approximately 30 % compared to a cantilever (figure 3.1).

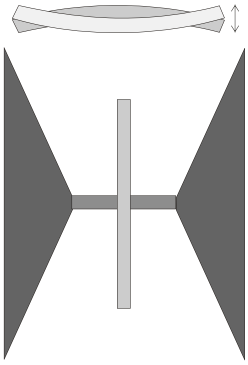

Figure 3.1 Designs to reduce clamping loss by Olkhovets

Wang *et al* [38] created a "free-free" beam with four torsional supports beam, each with a length of a quarter of the resonant frequency of the free-free beam. Since as a result of this design the torsional beams do not move at their support, no energy is dissipated into the support structure. The Roukes group [47] used a torsional double resonator to decouple the center resonator from its support.

3.4 Phonon-Phonon Scattering

Phonon-phonon scattering takes place if the oscillatory wavelength is considerably larger than the mean free path of phonons. The photons due to the oscillation (sound-waves) of the structure can interact with the phonons due to thermal vibration [47]. These sound-waves locally change the thermal-phonon frequencies and energy is dissipated to restore the equilibrium. The values for ωQ are found to be in the order of 10^{12} to 10^{14} for aluminum at 4.2 K and room temperature respectively. This process is an intrinsic process that will limit the largest possible Q-factor.

3.5 Phonon-Electron Scattering

In metals a free electron gas is present. Due to the external periodical force the ions start to oscillate which produces a varying electric field. The oscillating electric field forces the electrons to move. An electron gas can be approximated as a viscous fluid [47], therefore energy is dissipated by the motion of the electrons. For aluminum the ωQ is found to be 3×10^{11} for 4.2 K and 5×10^{13} for 4.2 K. However, an intrinsic semiconductor at room temperature has electrons and holes through thermal excitation. The external strain can change the band structure so that electron can migrate from one band to another. When an electron jumps from one band to another energy is dissipated. As with photon-photon scattering, electron-photon scattering is also a Q-factor limiting process.

3.6 High temperature background

In experiments, it is observed that at a transition temperature, the damping curve raises continually to a very large value until the melting point of the material is reached. This high temperature background is much smaller for single crystals than for polycrystals and it is smaller for samples with larger grains. This background might be due to a coupled relaxation behavior where stress relaxation across viscous slip bands takes place. The shorter slip bands relax first and as the longer ones start to relax additional stress can be put on the shorter bands.

3.7 Surface related effects

Carr [25] observed a linear relationship between the damping and the surface-volume ratio. Yasumura *et al* stated in a literature review that the Q-factor decreased with decreasing oscillator dimensions [58]. This suggests that the dominant loss mechanisms are surface related in NEM resonators. Unfortunately, loss mechanisms at the surface are still not well understood. A few possible mechanisms are proposed here.

3.7.1 Thin film on surface

Pohl's group [59] developed a method to obtain the quality factor of a thin film by depositing a film on a centimeter scale silicon double oscillator, and then measuring the Q-factors of the oscillator with and without the film. The relationship between the Q-factors is given as

$$\frac{1}{Q_{film}}=\frac{G_{Si}t_{Si}}{3G_{Film}t_{Film}}\left(\frac{1}{Q_{Paddle\ and\ Film}}-\frac{1}{Q_{Paddle}}\right)=\frac{G_{Si}t_{Si}}{3G_{Film}t_{Film}}\frac{1}{\Delta Q} \qquad 3.18$$

where G_{Film} and G_{Si} are the rigidity modulus and t_{film} and t_{Si} the thickness of the deposited material and Silicon respectively. All their measurements were taken at low temperatures ($T < 2K$). They found that the Q-factor of the film is similar to the one in bulk material. But they observed that the Q-factor of a SiO_2 film already differs significantly from the bulk at 10 K. The results suggest that for higher temperature, a more complex interaction between the two layers takes place and increases the losses.

3.7.2 Metal layer

To increase the conductivity of the resonator, a thin metal layer is deposited on the resonator. Evoy *et al* [34] [60] found that the quality factor decreases linearly with the thickness of this metal layer. From equation 3.18 it can be seen that this is expected:

$$\frac{1}{Q_{Paddle\ and\ Film}}=\frac{3G_{Film}t_{Film}}{G_{Si}t_{Si}}\frac{1}{Q_{film}}+\frac{1}{Q_{Paddle}} \qquad 3.19$$

But there is no dependence of the surface-volume ratio so it cannot explain the dependence of the Q-factor on the surface-volume ratio.

3.7.3 Oxide layer

A thin amorphous layer of oxide is formed if a silicon device is exposed to air. The layer is approximately 2.5 nm thick [25]. Since SiO_2 needs twice the space that silicon does, additional stress is created at the interface, which results in additional thermoelastic losses (paragraph 4.2). Removing the SiO_2 and all surface contamination by heat treatment increases the Q-factor by almost a factor of 5 [61]. Terminating the surface with hydrogen further increases the Q-factor. The hydrogen reduces the stress on the surface. If the thickness of the resonator is 200 nm, as in our experiments, the ratio of the film thickness and the resonator is $t_{film}/t_{sub} \approx 10^{-2}$. For this ratio of a SiO_2 layer with the substrate the Q-factor of the system decreased by around $\Delta Q \approx 10^5$ compared to the paddle without a SiO_2 layer [59]. From equation 3.18 we see that

$$\frac{1}{Q_{Paddle\ and\ Film}} = \frac{1}{\Delta Q} + \frac{1}{Q_{Paddle}} \qquad 3.20$$

The Q-factor of a 200 nm thick resonator to 10^5 at 1.3 K. In quartz glass (SiO_2) it is assumed that the Si-O bond length changes if an external stress is applied. The longitudinal oscillation of the bridging oxygen atom, resulting from an oscillating stress, dissipates energy [41]. Since the oxide layers on silicon NEM resonators also contain Si-O bonds, this process can also take place there.

3.7.4 Water layer

On a silicon surface with its native SiO_2 layer, a water layer of around 10 nm can be found (in normal atmosphere) [79]. Since water increases the internal friction of glass (SiO_2) by forming vibrating Si-OH groups [78], it is most likely that it also increases the losses in silicon NEM resonators.

3.8 Summary

Since photon-photon scattering and photon-electron scattering related losses are very small and NEM resonators have a relatively low quality factor, this effect can be neglected in NEM resonators. Air friction can easily be limited by performing the experiments in a good enough vacuum (p<< 1 mtorr). The influence of clamping losses in silicon resonators is highly controversial. Since the rhodium NEM resonator is clamped to the bonding pad, it is expected that clamping losses contribute much more to the total energy dissipation than in silicon NEM resonators. The structures used in this work have a high surface-volume ratio, therefore it is expected that surface related loss mechanisms are dominant [33] [58].

4 Stress relaxation

Energy dissipation is a strong function of temperature. At different temperatures different mechanisms can be dominant. Most mechanisms show a dissipation peak with a specific activation energy and relaxation time. This process is also called Debye relaxation. Since a relaxation time and an activation energy can be attributed to each relaxation mechanism, it is possible to compare the dominant loss mechanisms between different resonators. This helps to understand and isolate the dominant loss mechanism of an NEM resonator.

Relaxation results from a transition between two configurations in a solid. In a resonator the transition is stress induced. This behavior can be illustrated by considering two states in a system with slightly different energy levels, separated by a potential barrier of height H. Before a stress is applied, the system is in its minimum energy state. If an external stress is applied to the system the energy levels change their position (figure 4.1), and the other state is energetically more favorable. If the system can overcome the energy barrier H a transition from state one to state two takes place. The system is relaxed and the energy difference between the two states is lost.

In this chapter relaxation will first be explained mathematically (4.1) and then different relaxation phenomena (4.2 to 4.4) will be discussed.

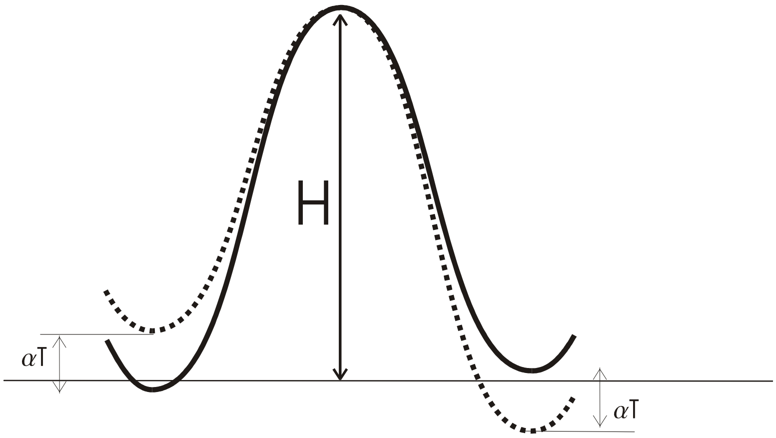

Figure 4.1 Influence of an applied stress to the energy levels of a system

4.1 Mathematical description of relaxation

To understand the relaxation behaviour of a material, a model needs to be found that describes its properties. Rheological models are a helpful tool to do so. They are the equivalent in elasticity to what equivalent circuit diagrams are in electrical engineering. [48].

In rheological models three elements are used: Hook's elements to describe elastic behaviour (figure 4.2a), Newton's elements to describe viscous damping (figure 4.2b), and St. Venant element for coulomb damping (figure 4.2c). The different elements can be connected either parallel to each other, then the strain is equal in both elements, or in series, then the stress in the two elements is equal.

The materials used in this work have a viscoelastic behavior. The simplest model to describe their stress relaxation and their creep behavior correctly is the Zener model. It consists of a Hook's element parallel to a Newton's element and an additional Hook's element in series. The stress strain relationship for this model is then

$$\sigma(t) + \frac{\eta_d}{E_s + E_p}\frac{d\sigma(t)}{dt} = \frac{E_s E_p}{E_s + E_p}\varepsilon(t) + \frac{E_p \eta_d}{E_s + E_p}\frac{d\varepsilon(t)}{dt} \qquad 4.1$$

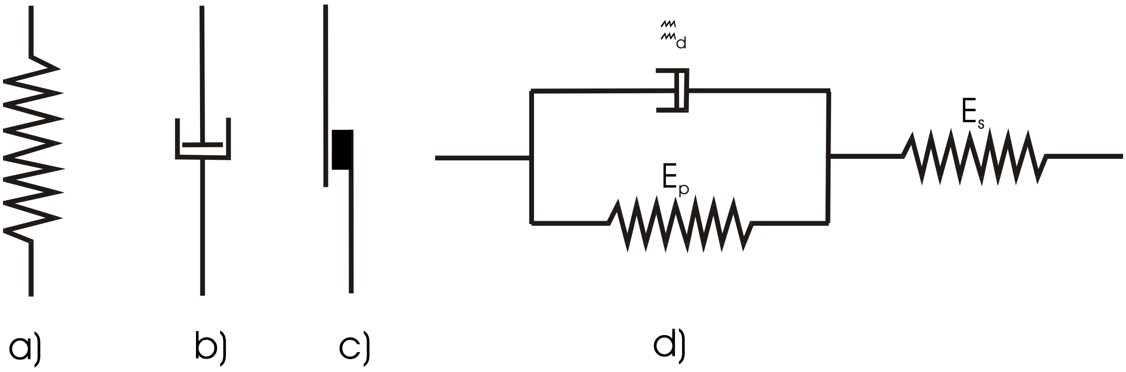

Figure 4.2 Hook's element (a), Newton's element (b), St. Venenat element (c) and the rheological representations of the Zener model (d)

From equation 4.1 the origin of the dissipation peaks can be explained. The following derivation is a summary of the one given in reference 49. For simplification the prefactors of equation 4.1are replaced by single constants.

$$a\sigma(t)+b\frac{d\sigma(t)}{dt}=c\varepsilon(t)+d\frac{d\varepsilon(t)}{dt} \qquad 4.2$$

To give some meaning to the constants in equation 4.2 in terms of relaxation two simple cases are considered: relaxation and creep. If a constant strain ε_0 is applied to a solid at time t=0, the stress-strain relationship (equation 4.2) becomes

$$a\sigma(t)+b\frac{d\sigma(t)}{dt}=c\varepsilon_0 \qquad 4.3$$

and has the following solution

$$\sigma(t)=\frac{c}{a}\varepsilon_0+\left(\sigma_0-\frac{c}{a}\varepsilon_0\right)e^{-\frac{a}{b}t} \qquad 4.4$$

The stress reaches its equilibrium at $\sigma=c/a\ \varepsilon_0$. Therefore, a relaxed Young's modulus $E_R=c/a$ can be introduced. Furthermore, a relaxation time $\tau_\sigma = b/a$ can be introduced. At $t=\tau_\sigma$ the stress is reduced to 36 % of its original value. If a constant stress σ_0 at t=0 is applied to the system, the stress-strain relationship becomes

$$\sigma_0=E_R\varepsilon(t)+E_R\frac{d}{c}\frac{d\varepsilon(t)}{dt} \qquad 4.5$$

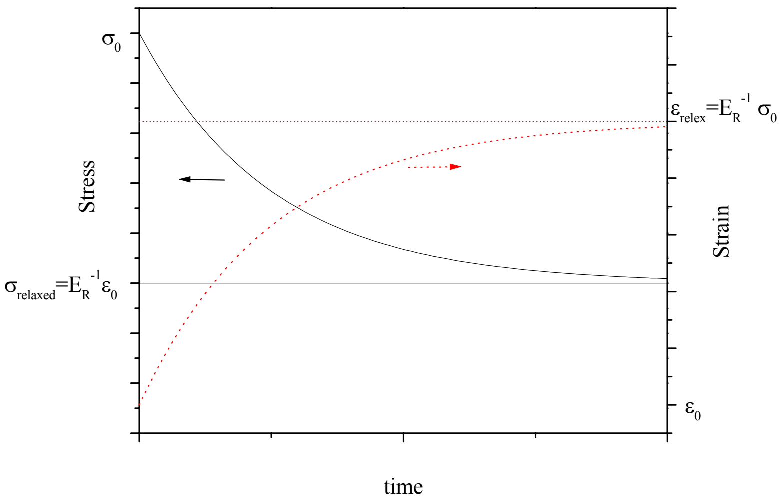

Figure 4.3 Stress relaxation and creep of a Zener solid

and has the following solution

$$\varepsilon(t)=\frac{1}{E_R}\sigma_0+\left(\varepsilon_0-\frac{1}{E_R}\sigma_0\right)e^{-\frac{c}{d}t} \qquad 4.6$$

The strain reaches its equilibrium at $\varepsilon=E_R^{-1}\sigma_0$. A strain relaxation time can be defined as τ_ε = d/c.

For further calculation it is helpful to define the modulus of the system at t=0. The so called unrelaxed modulus E_u, is given as

$$E_u=\frac{\tau_\sigma}{\tau_\varepsilon}E_R \qquad 4.7$$

if a periodical stress $\sigma(t)=\sigma_0\exp(i\omega t)$ is applied to the system. Neglecting the phase shift, the strain response can then be found as $\varepsilon(t)=\varepsilon_0\exp(i\omega t)$ and the stress-strain relationship (equation 4.2) can be rewritten as

$$(1+i\omega\tau_\varepsilon)\sigma_0=E_R(1+i\omega\tau_\sigma)\varepsilon_0 \qquad 4.8$$

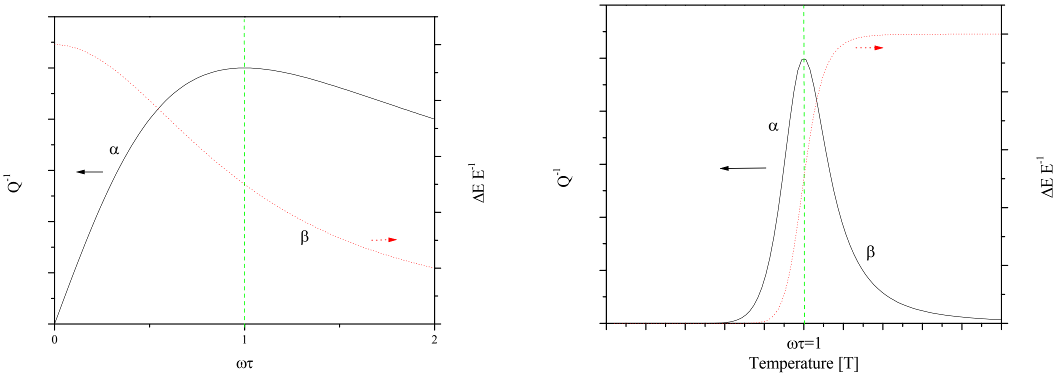

a) b)

Figure 4.4 $\omega\tau$ (a) and temperature (b) dependence of the Debye relaxation curves for internal friction (α) and dynamic modulus (β)

From equation 4.8 it can be found that the stress is related to the strain by a complex modulus Ê.

$$\hat{E} = E_R \frac{1+\omega^2\tau_\sigma\tau_\varepsilon + i(\tau_\sigma - \tau_\varepsilon)}{1+\omega^2\tau_\varepsilon{}^2} \qquad 4.9$$

The complex part of the modulus Ê is equivalent to the damping factor (paragraph 2.3). The inverse of the Q-factor is therefore

$$\frac{1}{Q} = \eta = \frac{\omega(\tau_\sigma - \tau_\varepsilon)}{1+\omega^2\tau_\sigma\tau_\varepsilon} = \frac{E_U - E_R}{E_0}\frac{\omega\tau}{1+(\omega\tau)^2} = 2\eta_{\max}\frac{\omega\tau}{1+(\omega\tau)^2} \qquad 4.10$$

Where τ is the average relaxation time $\tau=(\tau_\varepsilon\tau_\sigma)^{1/2}$, E_0 the average modulus $E_0=(E_\varepsilon E_\sigma)^{1/2}$ and $\eta_{\max}$ the maximal damping coefficient. The damping is maximum for $\omega\tau=1$. From equation 4.10 the relaxation strength Δ_E can be defined as

$$\Delta_E = \frac{E_U - E_R}{E_0} \qquad 4.11$$

The real part of the modulus (Ê) depends also on the frequency and on the strain relaxation time.

$$E = E_R \frac{1+\omega^2 \tau_T \tau_S}{1+\left(\omega \tau_S\right)^2} = E_U - \frac{E_U - E_R}{1+\left(\omega \tau_S\right)^2} \approx E_U - \frac{E_U - E_R}{1+\left(\omega \tau\right)^2} = 2\eta_{\max} \frac{1}{1+\left(\omega \tau\right)^2} \qquad 4.12$$

In an experimental setting with measurements over a wide range of ωτ, τ_S can be approximated with τ ($\tau_S \approx \tau$). The change of the modulus is then

$$\frac{\Delta E}{E} = 2\eta_M \frac{1}{1+\left(\omega \tau\right)^2} \qquad 4.13$$

For most relaxation phenomena the relaxation time is an exponential function of the temperature and can be described with an Arrhenius-type equation

$$\tau(T) = \tau_0 e^{\frac{H}{kT}} \qquad 4.14$$

H is the activation energy, any temperature dependence of H can be incorporated into τ_0.

The dissipation peak at ωτ=1 can be understood quantitatively in the following way [42]: If the vibration period is much larger than the relaxation time (ω<<1/τ), the system stays almost exclusively in equilibrium and not much energy is dissipated. If the period is much smaller than the relaxation time (ω>>1/τ), the system then does not have any time to relax and again not much energy is dissipated.

In real materials a deviation of the relaxation peak from the symmetric Debye peak can often be observed. This is either due to a distribution of relaxation times for one relaxation mechanism or to different relaxation phenomena lying close together and overlapping each other. A distribution of relaxation times can result from inhomogeneities in the material or from a different stress in the center than on the surface.

4.2 Thermoelastic relaxation

If the resonator is deformed, different areas experience different strains. Since stress and strain are coupled with temperature and entropy, the beam will then have a non uniform temperature distribution. Heat will flow from the high temperature regions to the low temperature regions and thus energy will be dissipated. Torsional modes do not suffer volume change and therefore no thermoelastic damping takes place [50]. Thermoelastic relaxation was first predicted and confirmed experimentally by Zener in 1937 and 38 [51] [52] [53]. Based on this work, Lifshitz developed a more accurate model to predict thermoelastic relaxation for a rectangular Euler-Bernoulli beam [42]. The following derivation follows reference [42]. The same coordinate system is used as introduced in paragraph 2.1. In consideration of thermal expansion the normal stresses in the beam are given by

$$\varepsilon_z = \frac{1}{E}\sigma_z + \alpha\Delta T \qquad 4.15$$

and the stresses in the other directions are

$$\varepsilon_x = \varepsilon_y = -\frac{\mu}{E}\sigma_x + \alpha\Delta T \qquad 4.16$$

where μ is the Poisson ratio and α the thermal expansion coefficient. All shear stresses are assumed to be zero. Following the same steps as in paragraph 2.1 the equation of motion can be obtained

$$\rho A \frac{\partial^2 u_x}{\partial t^2} + \frac{\partial}{\partial z^2}\left(EI_y \frac{\partial^2 u_z}{\partial z^2} + E\alpha I_T \right) = 0 \qquad 4.17$$

where I_T is the thermal inertia that can be defined as

$$I_T = \int_A x\Delta T dxdy \qquad 4.18$$

The heat equation in the presence of thermoelastic coupling in y-direction is given as

$$\left(1+2\Delta_E\frac{1+\mu}{1-2\mu}\right)\frac{\partial\Delta T}{\partial t}=D_{th}\frac{\partial^2\Delta T}{\partial x^2}+y\frac{\Delta_E}{\alpha}\frac{\partial}{\partial t}\frac{\partial^2 u}{\partial x^2} \qquad 4.19$$

where Δ_E is the relaxation strength:

$$\Delta_E=\frac{E\alpha^2T_0}{C_P} \qquad 4.20$$

C_P is the heat capacity per unit volume at constant pressure. Assuming that the heat transfer is fast enough such that the temperature changes follows the displacement without a time delay, the frequency can be found as

$$\omega=\omega_0\sqrt{1+\Delta_E[1+f(\omega)]} \qquad 4.21$$

Where ω_0 is the resonant frequency for a beam without thermoelastic losses (equation 2.28) and f (ω) is

$$f(\omega)=\frac{24}{t^3k^3}\left[\frac{tk}{2}-\tan\left(\frac{tk}{2}\right)\right] \qquad 4.22$$

with k

$$k=\left(1+i\right)\sqrt{\frac{\omega}{2D_{Th}}} \qquad 4.23$$

where t is the thickness of the beam and the D_{Th} is the temperature dependent diffusion constant

$$D_{th}=D_oe^{-\frac{H}{kT}} \qquad 4.24$$

Using a square root extension and neglecting all higher order terms the dispersion relation becomes

$$\omega=\omega_0\left[1+\frac{\Delta_E}{2}[1+f(\omega)]\right] \qquad 4.25$$

and the Q factor can be found as

$$\frac{1}{Q}=2\left|\frac{\mathrm{Im}(\omega)}{\mathrm{Re}(\omega)}\right|=\frac{E\alpha^2T_0}{C}\left(\frac{6}{\xi^2}-\frac{6}{\xi^3}\frac{\sinh\xi+\sin\xi}{\cosh\xi+\cos\xi}\right) \qquad 4.26$$

with

$$\xi=t\sqrt{\frac{\omega_0}{2D_{Th}}} \qquad 4.27$$

We see a strong dependence of the quality factor on the thickness of the beam. The thermoelastic relaxation peak can be seen more direct from Zener's original work, where he started from equation 4.1 and found the Q-factor for a rectangular beam as:

$$\frac{1}{Q}\approx\frac{E_{ad}-E}{E}\frac{\omega\tau}{1+\omega^2\tau^2}=\frac{E\alpha^2T_0}{c_\sigma}\frac{\omega\tau}{1+\omega^2\tau^2} \qquad 4.28$$

with

$$\tau=\frac{a^2}{\pi^2D_{th}} \qquad 4.29$$

Cavities and other impurities or grains with different crystal orientations introduce a non-uniform stress distribution even if no external stress is applied. This non-uniform stress distribution increases thermoelastic losses. A mathematical proof would be beyond the scope of this thesis but is given by Zener [52]. The concept of thermoelastic losses fails if the length of the beam is smaller than the mean free path of a thermal photon. [54]

4.3 Defect Relaxation

Point defects in crystals produce a local non-uniform stress distribution [50]. It is possible to associate a symmetry with each defect. If the defect symmetry is lower than the crystal symmetry, an elastic dipole originates. Consequently, there will be an interaction between the dipole and a homogeneous applied stress and if an activation energy is overcome, a reordering of the dipoles take place.

In bcc metals, the dipole is introduced by interstitial impurities (Snoek relaxation) [50]. The interstitial atoms occupy the octahedral sites and have a four-fold symmetry (tetragonal symmetry). When a dipole reorientates the interstitials jump to the neighboring octahedral site. It can be found that the activation energy that controls the relaxation time is similar to the one for the migration of the interstitials.

Zener relaxation is observed in over 20 alloy systems and in all three common metallic structures [50]. The relaxation is due to a stress-introduced reorientation of atom-defect pairs in the nearest neighbor configuration. The atom-defect pair can be considered as a dumbbell that rotates about its center. The concept of defect pairs applies only to solids with a high impurity concentration. In silver the peak starts to be become visible at a zinc impurity of about 3.7 % and increases significantly with zinc concentration.

The simplest model to describe dislocation relaxation is to consider the dislocation as a loop that is firmly pinned at its end and executes vibration under an external periodical stress (like a vibrating string) [50]. A major limitation of this model is that stresses and strains outside the slip plane are neglected. The pinning points are assumed fixed, which is only true at low temperatures, where the diffusion is negligible. Dislocation damping can be nonlinear and shows a strong amplitude dependence.

4.4 Grain boundary relaxation

In a polycrystalline material the grains slide back and forth if a periodical stress is applied. Since friction occurs if two grains are sliding along each other, energy is dissipated [55]. The sliding is blocked at the end of the grain but can be continued if the strain is large enough to overcome the blocking. The activation energy of grain boundary relaxation lies between the activation energy of volume diffusion and of grain boundary diffusion, which suggests that boundary relaxation is linked to diffusion. The grain boundary consists of many disordered atom groups, separated by regions where the atoms fit (figure 4.5).

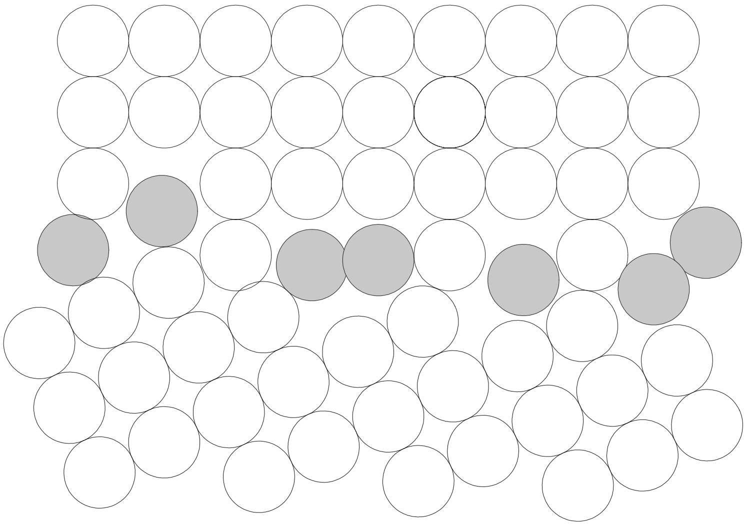

Figure 4.5 Schematic illustration of a disordered atom group model

The stress at the shaded atoms in figure 4.5 differs from the stress of the atoms around them. The disordered atoms can pass over each other by squeezing the atoms around them. This displacement has components parallel and perpendicular to the grain boundary and is therefore accomplished by a combination of sliding and migration. Migration is a volume diffusion process and sliding is a grain boundary diffusion process. Hence the activation energy for grain boundary relaxation is expected to be somewhere between the two activation energies. The macroscopic grain boundary sliding between two grains results from the summation of the atomic rearrangement in various disordered groups. The coefficient of viscosity of grain boundary sliding is similar to that of molten metal [56]. For larger grains the relaxation peak shifts towards higher temperatures, but its height stays approximately the same [57]. Since a larger displacement can take place before the sliding is blocked by the grain edge for larger grains, the relaxation time increases. In a given volume the grain surface (S_{grain}) is proportional to the to reciprocal of the grain size ($S_{grain} = \alpha / d_{grain}$).

The energy dissipation for each grain (E_{grain}) is proportional to the displacement at the grain boundary and the maximum displacement is proportional to the grain size ($E_{grain}=\beta\, d_{grain}$). The total dissipated energy (ΔE) in a given volume is then

$$\Delta E = E_{grain} S_{grain} = \alpha\beta \qquad 4.30$$

where α and β are constant. From equation 4.30 it can be seen that the total dissipated energy is independent of the grain size.

4.5 Summary

Thermoelastic and defect related losses will be present in NEM resonators, but it is expected that they are not dominant and do not show a relaxation peak in the temperature range available in this work [33]. Grain boundary related losses play an important role in the rhodium samples. Since grain boundary peaks are at higher temperatures [55]-[57] it is not possible to investigate grain boundary relaxation in this work.

5 Device fabrication and setup

The fabrication of NEMS involves electron beam lithography (EBL), metal deposition, RIE and wet etch processes. This project involved the installation of an EBL system at Virginia Tech. Once the EBL tool was installed and preliminary pattern had been written, the NEMS fabrication process originally developed at Cornell [65] [25] was optimized for the equipment available at Virginia Tech by William Barnhart [64].

The characterization of NEM resonators requires an experimental test bed offering sub-nanometer deflection detection sensitivity. Since no commercial system is available, this project also involved the building of such a system. Paragraph 1.4 will outline different detection methods, and will justify our choice of the specific technique chosen for this work.

5.1 Electron beam lithography

In electron beam lithography (EBL), a beam of electrons is scanned across a resist-covered surface [62]. The electrons change the chemical structure of the resist. In positive resists, the electrons break the polymer chains of the resist. After developing, the exposed parts are dissolved, while the rest of the resist stays on the surface. In a negative resist, however, the polymer chains are cross-linked by the electrons. In this case, the exposed resist remains therefore on the surface, while the unexposed is dissolved in the developing solution.

Since the wavelength associated with electrons is much smaller than those of photons (2 Å for electrons with an energy of 30 keV), the exposure resolution is no longer limited by diffraction as in optical lithography, but rather by electron scattering events in the resist. For instance, PMMA has an intrinsic resolution limit of 10nm.

Quick turnaround times and the ability to write patterns in the submicron region makes EBL a very versatile tool that is widely employed in research and development. It is also commonly employed for the fabrication of masks for optical lithography systems.

5.1.1 Electron-Solid-Interaction

When the electrons interact with the resist, they get scattered [62]. Small angle scattering events, also known as forward scattering, results in an enlargement of the beam diameter. The enlargement of the beam is empirically found as

$$\Delta d = 0.9\sqrt{\frac{t_{\mathrm{Resist}}}{\mathrm{V}_{\mathrm{acceleration}}}} \qquad 5.1$$

where t_{resist} is the resist thickness in nanometers and $V_{\mathrm{accelration}}$ the beam voltage in kilovolts. Using the highest available acceleration voltage and the thinnest possible resist increases the resolution of the lithography. The thickness of the resist cannot be reduced arbitrarily, because the steps following the lithography need a certain resist thickness (i.e. the resist must be thicker than the metal layer that is deposited in the next step). Electrons also undergo large angle scattering, also known as backscattering. This happens especially in the substrate due to its higher density compared with the resist. Backscattered electrons result in an exposure of the resist from its rear, therefore an adjustment of the dose is required to prevent overexposure. This effect is called the proximity effect. The fraction of electrons that backscatter is roughly independent of the beam energy but depends strongly on the substrate material. The percentage of backscattered electrons ranges from 17% for silicon to 50% in tungsten. Finally, when the electrons slow down, a cascade of low voltage secondary electrons is created. Secondary electrons have energy between 2 and 50 eV. They do the bulk of the exposure, but also widen the beam by roughly 10 nm. Figure 5.1 is a simulation of the scattering of the electrons and shows how the acceleration voltage affects the EBL resolution.

5.1.2 Strategy to avoid the proximity effect

The interaction between the resist and the electron can be simulated prior to writing. The dose can then be adjusted for each part of the pattern so that the whole structure is exposed equally with the same dose. The required calculations are complex and time-consuming. A correction method where no calculation is required is the GHOST method. Here the inverse shade of the pattern is written with a defocused beam to imitate backscattering for the areas that experience less backscattering. After the structure is written the whole writing field was exposed to the same background dose. Expensive stand alone EBL systems have either dose modulation or GHOST built in, while in low cost systems the proximity effect can only be corrected manually, by assigning different doses to different parts.

Another approach to reduce proximity effect is to use a multilayer resist where a first thin layer is sensitive to electrons, while the second thicker layer is not. The thick layer absorbs all backscattered electrons, so that they cannot damage the top layer. The pattern from the thin layer is transferred into the thicker layer using a dry etching process.

5.2 Virginia Tech EBL system

The system installed at Viginia Tech is the Nanometer Pattern Generation System (NPGS) from J. C. Nabity Lithography Systems. This pattern generator was installed as an add-on module to a pre-existing LEO 1550 SEM. This system is based on a Windows PC with a data translation DT2823 multifunction board (DAC). The board is used to generate the X and Y beam deflection [62]. NPGS controls the stage and other microscope settings via the serial port. The ISA-bus limits the deflection speed to around 100 kHz, which is equivalent to a minimum dwell time of 10 μs per point. The NPGS uses a vector scan method, where the view field is sectioned in single pixels. Each shape is filled by rastering the beam along the pattern. A limitation of this SEM based system is the absence of a high tech laser stage, which reduces the maximum structure size to the view field. Due to the size of our structures this is not a problem.

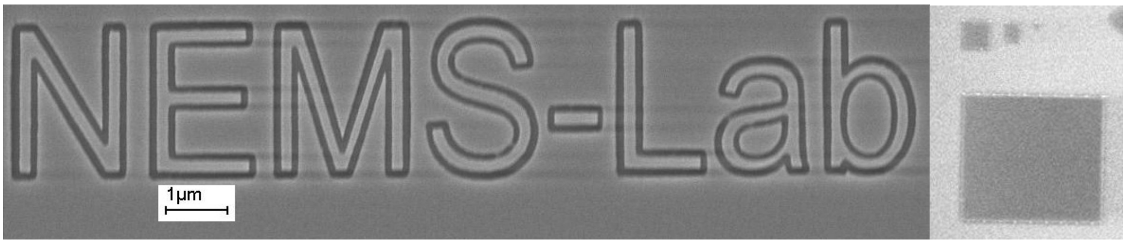

a) b)

Figure 5.1 First structure written with EBL at Virginia Tech a) using NPGS b) using the SEM alone, PMMA as negative resist.

5.3 Surface machining of NEMS

The starting material for surface machine NEMS is a silicon-on-insulator-wafer (SOI). The wafer used in this research had a 350 nm thick <100> orientated and boron doped (resistivity ~14 Ω cm^{-1}) top silicon layer. A 400 nm insulating SiO_2 layer was followed by a 500µm thick intrinsic silicon substrate (resistivity ~230,000 Ω cm^{-1}).

After the wafer was cleaned with acetone and isopropyl alcohol (IPA) the resist was deposited using a spin coater. A two layer resist was used. First a low weight PMMA (496k) diluted in 5% anisole was spun for one minute at 4000 rpm. Afterwards, the wafer was baked for 15 minutes on a hotplate at 170°C to remove the excess solvent. After the wafer was cooled down, a second layer of resist of higher molecular weight PMMA (950k) diluted in 4% anisole was deposited with the same speed and also backed. The total thickness of the resists varied between 340nm and about 430nm. The low weight PMMA is more sensitive to electrons than the higher weight PMMA, so an undercut is created, which makes the metal lift off easier. The second layer also fills the pinholes of the first layer.

In the next step the pattern was written with the NPSG-EBL system at the highest possible acceleration voltage (30 kV). The dose was varied between 170 µC/cm^2 for the large features and 250 µC/cm^2 for the smaller features. The lines were written with a dose of around 5 nC/cm. After the exposure the structure was developed in a 1:3 IPA:Methyl isobutyl ketone (MIBK) for 70s with mild agitation. After developing approximately 50 nm aluminum was evaporated onto the sample. In a next step the remaining resist with the aluminum on top was washed away using a solution of equal parts acetone and dichloromethane for 5 minutes in an ultrasonic bath. The remaining solvents are removed from the surface by putting the sample for a short time in IPA in an ultrasonic bath. After the resist is dissolved, the aluminum in the desired structure is left. The structure can be transferred into the Silicon using a dry etch process.

Finally the structure is released by removing the SiO_2 underneath the structure. This is done by dipping the sample in Buffered Oxide Etch (BOE) (hydrofluoric acid 1:10). BOE etches away approximately 50 nm a minute. BOE also etches aluminum and due to its small thickness all the aluminum was etched away. Finally the chip can be wirebonded to the sample holder. It is important to keep in mind that during the whole fabrication process no liquid may dry on the surface. The sample has to be kept wet when going from one solution to another and blown or spun dry afterwards.

5.4 Testing of nanomechanical structures

Since the NEM resonators are expected to resonate in the MHz regime with a resonant amplitude in the nanometer regime, subnanometer displacement detection is required. Different detection methods with a subnanometer resolution are reported in literature. In the following section they will be reviewed and their advantages and disadvantages will be discussed.

5.4.1 Capacitive detection

The capacitance of a plate capacitor, neglecting edge effects is given as

$$C = \frac{\varepsilon_0 A}{d} \qquad 5.2$$

where A is the area of the plates and d the distance between the two plates. From this equation it can be seen that if the distance of the two plates changes so does the capacitance [25]. The paddles used in this research had a width (w) of 2 μm and a length of 3.5 μm. The distance between the paddle and the substrate was 400 nm. The resulting capacitance (C_{paddle}) is 1.5 10^{-16} F. The change in the capacitance for a change in the distance (Δd) is given as

$$\Delta C = C\frac{\Delta d}{d} \qquad 5.3$$

For a maximum deflection of 1 Å the change of capacitance is then ΔC= 3.8 10^{-20} F. The bonding pad has a size of 100μm x 100μm and has a capacity of 8.6 10^{-13} F (ε_{SiO2}=3.9ε_0). The two capacitances are parallel to each other, so the total capacitance of the system is 8.6 10^{-13} F. This means that to detect a 1 Å deflection, a change in capacitance in the order of 10^{-6} % has to be detected. No equipment is available to detect this change in capacitance, especially in the RF frequency range [66].

For a thin, good conducting resonator with a high quality factor vibrating laterally, calculations have shown that it is possible to pick up the resonance capacitivly, but an experimental observation is missing so far [64].

5.4.2 Magnetic detection

This method makes use of the Lorentz force [67]. If a current flows through a wire that is exposed to a perpendicular magnetic field, a force acts on the current and the wire moves perpendicular to the magnetic field. Since the current is oscillating the wire also oscillates and an electromotive force (EMF), having the same frequency, is induced in the wire. To pick up the vibration either the reflected voltage can be measured with a network analyzer [69], or the electromagnetic power that is absorbed by the motion of the beam can be measured [67]. To excite the resonator, relatively large magnetic fields are required (up to 12 Tesla [67]). Since the experiment has to be performed at cryogenic temperatures [25], this method is not suitable for temperature dependent measurements. Another drawback of this method is that in order to prevent heating the structure has to have low resistance [25]. For a silicon resonator this can only be accomplished with heavy doping or a thick metal film on top of the resonator, which makes this method unsuitable if the intrinsic characteristic of silicon is of interest.

5.4.3 Electron beam detection

If the secondary electron detector of an SEM is coupled with a spectrum analyzer, an SEM can be used to detect lateral vibration of a resonator [69]. The electron beam is focused at the edge of the resonator. If the resonator vibrates it moves in and out of the electron beam, so that the signal at the detector changes at the frequency of the resonator. To get a good contrast the silicon underneath the beam has to be removed. This method was successfully used to measure the resonant frequency of a 200 μm long beam resonating in the 100 KHz regime. The minimum detectable deflection of an SEM in a low noise environment is approximately two nanometers. Since the maximum deflection of a NEM resonator is in the nanometer region, it might be difficult to pick up the vibration. This method is not suitable if the resonator vibrates vertically.

5.4.4 Optical detection methods

The frequency of a light source changes with the speed of the light source (Doppler effect). Since the reflective surface of the resonator can be considered as a point source, this effect can be employed to detect the vibration of a resonator. The change of frequency can be detected with a Doppler vibrometer. This method was successfully used by Yasumura [58] and Yang [61] for the vibration measurement of micron scale cantilevers. A Doppler system would work perfectly on a paddle resonator with a relatively high displacement but not with cantilevers or beams. Since a cantilever is much smaller than the laser beam most of the reflected light would not have the shifted frequency. To detect the vibration in commercially available Doppler Vibrometers it is necessary that most of the reflected beam has the shifted frequency [70].

The most common optical method to detect displacement of a micronscale cantilever is to use a position-sensitive detector (PSPD). This method is implemented in most AFMs. A laser is reflected off the end of a cantilever, and depending on the angle between the surface of the cantilever and the incident laser beam, the position of the reflected light at the detector changes. The detector can measure displacements of a light beam in the

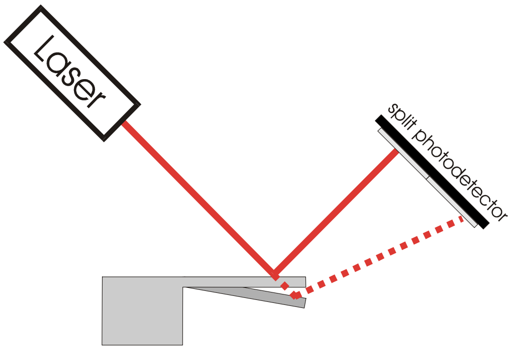

Figure 5.2 Principle of a deflection system used in an AFM and change of reflection of a beam

nanometer scale, which is equivalent to a displacement of the cantilever in the sub-angstrom scale [11]. Since in the translational mode the paddles stay almost parallel to the substrate, the displacement at the detector is similar to the displacement of the paddle, which might be to small for the detector. The cantilevers and clamped beams are much smaller than the spot size of the laser beam; therefore most of the signal at the detector does not change its position at all. However no high-speed PSPD's are available [25].

5.4.5 Interferometry method

Before PSPD detectors were used in AFMs, a detection method based on a Farby-Perot interferometer was used. In a Fabry-Perot interferometer the reflected light from two consecutively parallel surfaces interfere. If the distance between the two surfaces changes periodically, so does the intensity of the light. Since NEM resonators are relatively thin, part of the light is transmitted through the structure and is reflected by the substrate. Therefore a NEM resonator acts as Fabry-Perot interferometers.

The principle of a Fabry-Perot interferometer is shown in figure 5.3, the incident light is not printed normal to the resonator to better visualize the different optical paths. This method was first used by Carr *et al* to detect the vibration of NEM resonators [25] [65].

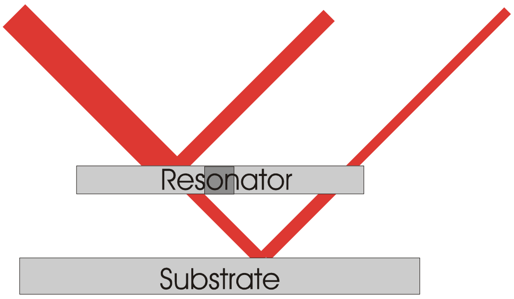

Figure 5.3 Principle of a Farby-Perot interferometer

A general disadvantage of optical techniques, as of interferometrical methods, is that the laser beam locally increases the temperature of the structure. The increase of temperature can be estimated as [71]

$$\Delta T = \frac{2P}{\pi^2 aK} \tag{5.4}$$

K is the thermal conduction ($K_{Si} = K_{Rh} = 150\ \mathrm{W\ m^{-1}\ K^{-1}}$) and P the absorbed power, which is 0.15 mW for a 200 nm thick silicon resonator and 0.6 mW for a 350 nm thick rhodium resonator. Hence, the average temperature increase of the silicon substrate will be 0.5 K, while the temperature increase of the rhodium substrate is 2 K. The temperature increase of the resonator is not uniform but will be different on the top and on the bottom; as a result additional stress is introduced in the structure, which decreases the Q factor (paragraph 4.2). The situation is even worse if the spot of the laser is smaller than the vibrating structure, because then the introduced stress on the surface will be inhomogeneous. For a disc resonator with a radius between 5 and 20 µm a frequency shift of 0.04% is observed if the laser power is increased from 100 µW to 250µW. That this shift is due to the non-uniform heating of the resonator was confirmed with a FEM simulation [34].

Due to its simplicity and its suitability for temperature dependent measurements the Fabry-Perot interferometer is used in this work. The experimental setup will be described completely in section 5.5.2.

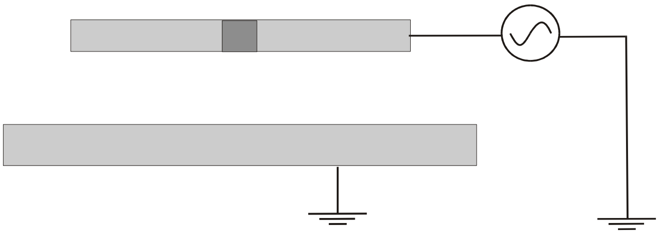

Figure 5.4 Electrostatical actuation

5.5 Experimental setup

5.5.1 Electrostatical actuation

The resonators were driven electrostatically. To attenuate the resonator an oscillating potential can be applied between the structure and the substrate (or between the resonator and an additional electrode). The structure can be approximated as a plate capacitor. The energy of a plate capacitor is given as

$$E = \frac{V^2(\omega t)C}{2} \qquad 5.5$$

The force between these two plates using the capacitance of a plate capacitor (equation 5.2) can be easily calculated

$$F = \frac{\partial E}{\partial h} = \frac{1}{2}V(\omega t)^2 \frac{\partial C}{\partial h} = -\frac{1}{2}\frac{\varepsilon_0 A}{h^2}V^2(\omega t) \qquad 5.6$$

where h is the distance between the two plates. Since the force is proportional to the square of the applied potential, the frequency of the force is twice the frequency of the potential. To obtain a force that has the same frequency as the applied voltage an additional DC signal can be added to the AC signal, which leads to a total potential of

$$V(\omega t) = V_{DC} + V_{AC}\cos(\omega t) \qquad 5.7$$

and a force of

$$F(\omega t) = -\frac{1}{2}\frac{\varepsilon_0 A}{h^2}\left(V_{DC}{}^2 + 2V_{DC}V_{AC}\cos(\omega t) + \left(V_{AC}\cos(\omega t)\right)^2\right) \qquad 5.8$$

If $V_{AC} \ll V_{DC}$ the term $V^2_{AC}\cos^2(\omega t)$ can be neglected and the force will oscillate with the same frequency as the potential around a force F_0. The DC potential not only creates a force offset but also increases the amplitude of the oscillation. Due to electrical losses the potential at the resonator is much smaller than the output potential of the power supply. Therefore a loss factor α will be introduced in equation 5.8. To simplify the discussion all prefactors were combined in one factor (F_{unit})

$$F(\omega t) = -\alpha \frac{1}{2}\frac{\varepsilon_0 A}{h^2}\left(V_{DC}{}^2 + 2V_{AC}V_{DC}\cos(\omega t)\right) = F_{unit}A\left(V_{DC}{}^2 + 2V_{AC}V_{DC}\cos(\omega t)\right) \qquad 5.9$$

5.5.2 Room temperature setup

Since the Fabry-Perot interferometer technique is successfully used to characterize NEM resonators [34] [65] and is relatively simple to build, the setup for this work is based on this technique. The laser was a 35 mW helium-neon laser (633nm) from JDS Uniphase, directly followed by a double concave lens with a focal length of –25 mm to widen the beam to uniformly illuminate the microscope objective. Approximately 16” away from the laser a 1” beam splitter cube was set up followed by a Olympus SLMPlan 20x microscope objective at 13” further. The objective had a numerical aperture of 0.35 and a working distance of approximately 2 cm. The sample was mounted in a CF 2 ¾” vacuum tee on an IC socket that was glued on a Teflon spacer. Four of the pins of the IC socket were connected to the 4 BNC feed-through at the back of the chamber. The ground was taken from the chamber walls. The tee was closed with a quartz window in the front and a valve at the side. The chamber was pumped down with a rotary pump below 10 mtorr before disconnecting the pump for the measurement. This was done to limit the vibration of the chamber during the measurements, but also to prevent the chamber from tilting since it was not screwed to the base plate but rested on a U shaped holder. We did not have the ability to monitor the pressure in the chamber itself. An xyz stage with a positioning sensitivity of about one micrometer was used to position the chamber.

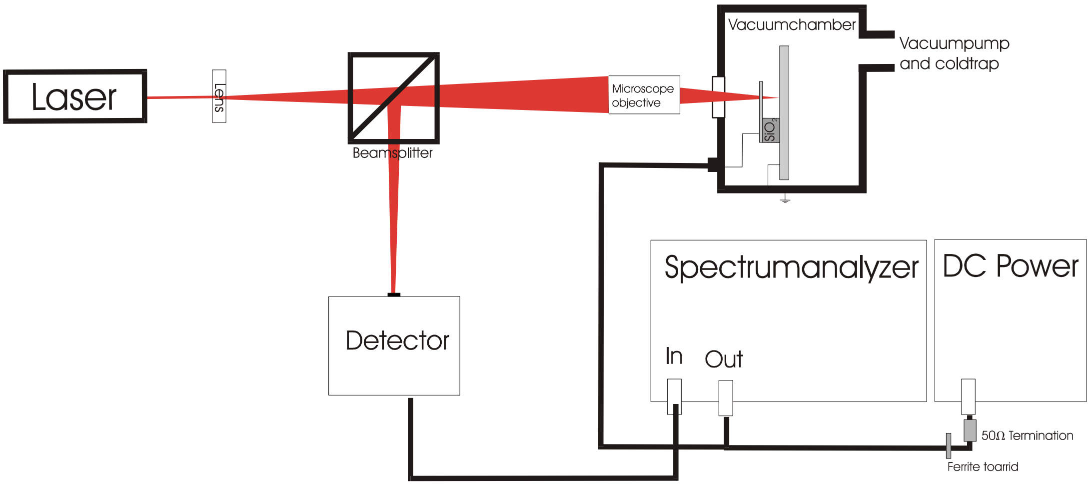

Figure 5.5 Experimental setup for room temperature measurements

The signal reflected from the sample was then directed from the beam splitter to the photo detector, located 9" away from the beam splitter. The AC coupled output of the detector was connected to the spectrum analyzer (HP E4411B). To align the beam a rectangular ocular could be placed between the detector and the beam splitter. A viewing screen with a butt was placed above the ocular.

The spectrum analyzer was used in the tracking mode, so its internal frequency generator was used to drive the structure. In this mode the spectrum analyzer measures at the same frequency as its output signal. To amplify the signal and to obtain a driving force with the same frequency as the output signal of the spectrum analyzer, a DC power supply (Kenwood Pac30-2) with a 50Ω terminator was connected parallel to the spectrum analyzer. Since the power supply acted as an antenna and picked up all kinds of noises, a ferrite toarrid was coiled around the output cable of the power supply. For better shielding, all cables, and also the detector, were wrapped with aluminum foil. The aluminum foil was connected to the optical table to ensure a uniform ground. The aluminum reduced the noise significantly.

5.5.3 Low temperature setup

The low temperature setup was used to measure the temperature dependence of the Q-factor from 50 K to room temperature. All components of the setup were the same as in the room temperature setup, only the vacuum chamber was replaced with a Janis CCS-

150 closed cycle cryostat. The accessible temperature of this cryostat ranged from 10 K to 300 K. Since the working distance of the microscope objective was around 2 cm, but the distance between sample holder and the viewing port was approximately 4 cm, a copper adapter was built to move the resonator closer to the window. The actual sample holder consists of a copper base plate and two copper electrodes isolated with a Teflon layer from the base plate. The chip with the resonator was clamped on the base plate with a metal clamp. The clamp made sure that the chip was tied and had good thermal contact with the sample holder. The thermocouples were screwed on the copper adapter as close as possible to the sample. The thermocouples were connected to a LakeShore 330 controller. The cold finger was directly attached to the displacer and since the displacer vibrated heavily so did the cold finger. The vibration was strong enough that even a rough alignment was impossible with the cryostat running, so it had to be turned off for the measurements. The temperature increase during the actual measurement was less than one Kelvin. The original vacuum connection to the chamber was a 1” long pipe with an outer diameter of a ¼”. Since the small inlet reduced the pumping speed in the chamber drastically, the top window of the cryostat was removed and an adapter was clamped onto the cryostat chamber. So the pipe diameter at every point was at least 2.3 cm. A Pfeifer turbo pump and a liquid nitrogen cold trap were used. A thermocouple and an ionization gauge, located outside the chamber were used to monitor the pressure of the system. The maximal vacuum that could be obtained was around 5 x 10^{-5} torr. The vibration of the pump was damped by running the vacuum tubing through sand. This damping is sufficient for alignment and for measurements, but for high quality measurements the pump had to be turned off. Due to the short measurement times and the cold trap, the vacuum was almost constant during the measurement. For electrical contact, the built-in BNC feed-through was used and the signal was connected to the chip using isolated single lead wires. The ground was obtained from the cold finger. In addition to the room temperature setup the spectrum analyzer and the temperature controller was connected to a Windows PC using a GPIB interface. A LabVIEW program was developed to save the data to the hard disk but also to adjust the settings of the spectrum analyzer. The LabVIEW program also performed the first data analysis, i.e. determining the resonant frequency and calculating the Q-factor using the estimation method (equation 2.68).

5.5.4 Modeling of optical response

The sensitivity of our experimental setup can be estimated by calculating the intensity of the two interfering signals. For a rough estimate, all higher order reflections can be estimated. The error can be estimated by looking at the first higher order reflectance. The reflectance at an interface is given as [72]

$$R = \frac{(n_2 - n_1)^2 + (k_2 - k_1)^2}{(n_2 + n_1)^2 + (k_2 + k_1)^2} \qquad 5.10$$

The transmitted intensity (T) at the interface is than

$$T = 1 - R \qquad 5.11$$

and the light absorbed by the resonator is given by

$$P = P_0 e^{-\frac{4\pi k}{\lambda} t} \qquad 5.12$$

In figure 5.6, I_0 is the intensity of the incident light, I_1 the intensity of the light I_2 is the intensity of the light transmitted through the resonator and reflected by the bottom side of the resonator. I_3 and I_4 are the intensities of the light reflected by the substrate. With the index of refraction of silicon n_{Si}=3.87 and the extinction coefficient k_{Si}=0.02 the intensities of the reflected light can be calculated (table 5.1).

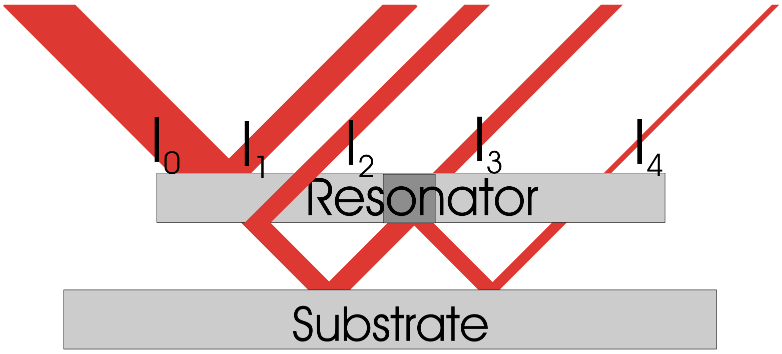

Figure 5.6 Higher order reflections of a Farby-Perot interferometer

	Intensity	
I_0	I_0	3 mW
I_1	0.347 I_0	1.04 mW
I_2	0.126 I_0	0.38 mW
I_3	0.054 I_0	0.16 mW
I_4	0.006 I_0	0.02 mW

Table 5.1 Intensity of the reflected light from the resonator

The intensity of the incident light I_0 can be estimated form the laser intensity (35mW) and the absorption of the optical components between the laser source and the device (Table 5.2) and can be found as $I_0 \approx 3mW$.

	Transmission coefficient
Lens	0.5
Beam splitter	0.3
Microscope objective	0.6
Cryostat window	0.9
Total absorption from laser to sample	0.08
Total absorption from sample to detector	0.16

Table 5.2 Absorption coefficient of the optical parts measured with a Filmetrics

For an estimate of the optical response of the system the intensity of the reflected light can be calculated by letting I_1 and I_3 interfere with each other. From table 5.1 it can be seen that this is a very rough estimate, but it should give the correct magnitude. Since I_1 and I_3 are both reflected once they have the same phase and the intensity can be calculated with equation 5.12 [72] .

$$I_{total} = I_1 + I_3 + 2\sqrt{I_1 I_3}\cos\left(\frac{2\pi}{\lambda} l_{optical}\right) \tag{5.13}$$

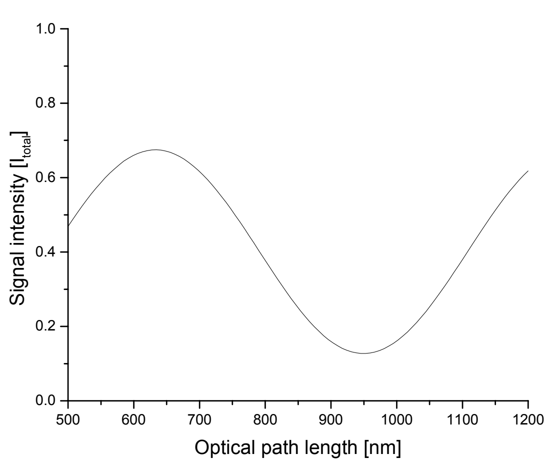

Figure 5.7 Change of intensity with a change of the optical path length

$l=l_{optical}$ is the optical path length between the two surfaces and can be calculated from

$$l_{optical} = \sum_i n_i s_i \tag{5.14}$$

s_i is the distance that the light travels through a material with an index of refraction n_i. For a 200 nm thick silicon resonator with a gap thickness of 400nm, the optical length is 1174 nm. The change of the reflected light with a changing optical path length can be seen in figure 5.7.

The change in intensity if the distance between the resonator and the substrate changes by Δx can be calculated from equation 5.13

$$\Delta I = 2\sqrt{I_1 I_3}\left(\cos\left(\frac{2\pi}{\lambda}l\right) - \cos\left(\frac{2\pi}{\lambda}(l+\Delta x)\right)\right) \tag{5.15}$$

For a deflection (Δx) of one angstrom intensity of the reflected light changes $\Delta I=2.1\ 10^{-4}\ I_0$ or approximately ΔI=630 nW. This results, due to the absorption of the optical components, in a signal of around 100 nW at the detector.

For the interpretation of the data, it is helpful to show that the signal intensity changes linearly with Δx for small deflection. Using a cosine expansion, equation 5.15 becomes

$$\Delta I = 2\sqrt{I_1 I_3}\left(\left(1-\alpha^2\frac{l^2}{2!}+\alpha^4\frac{l^4}{4!}+\dots\right)-\left(1-\alpha^2\frac{(l+\Delta x)^2}{2!}+\alpha^4\frac{(l+\Delta x)^4}{4!}+\dots\right)\right) \tag{5.16}$$

where $\alpha=2\pi\lambda^{-1}$. Since $\Delta x \ll 1$ all higher order terms of Δx can be neglected, equation 5.16 becomes

$$\Delta I = 2\sqrt{I_1 I_3}\begin{pmatrix}\left(1-\alpha^2\frac{l^2}{2!}+\alpha^4\frac{l^4}{4!}+\ldots\right)-\left(1-\alpha^2\frac{l^2}{2!}+\alpha^4\frac{l^4}{4!}+\ldots\right)\\ +\Delta x\left(\alpha^2\frac{2l}{2!}-\alpha^4\frac{4l^3}{4!}+\ldots\right)\end{pmatrix} \qquad 5.17$$

or simply

$$\Delta I = 8\sqrt{I_1 I_3}\,\frac{\pi^2}{\lambda^2}\Delta x\left(\alpha^2\frac{2l}{2!}-\alpha^4\frac{4l^3}{4!}+\ldots\right) \qquad 5.18$$

5.5.5 Sensitivity of the Detector

The detector used for this work was a 1 GHz low noise detector from New Focus (model 1601). The detector has a noise-equivalent power (NEP) of 38 pW/Hz$^{-1/2}$ and a gain of 300 V/W at 633 nm. The bandwidth (BW) of the spectrum analyzer was 5 kHz. The minimum detectable signal can be calculated as a product of NEP and BW$^{1/2}$ and is therefore 2.6 nW, which would yield in an electrical signal of 0.8 μV. Since the noise level of the electrical equipment is in the same magnitude, intensity changes of the signal larger than 3 nW can be detected. A deflection of 1 Å results in an intensity change of ΔI =100 nW at the detector or a signal of 30 μV. The setup is therefore sufficient to detect sub-nanometer scale motion, even if structure is much smaller than the diameter of the incident laser beam.

5.5.6 Electrical calibration

Since cables and connecters have frequency dependent losses, the electrical losses of the system were measured. This measurement also helped to determine the impact of a 50Ω terminator at the power supply and the capacitor for impedance matching at the feed-through to the vacuum chamber. Since the non-shielded cables in the low temperature setup are longer than in the room temperature setup, the calibration measurements are only performed for the low temperature setup. The setup was wired, as it would be done for a regular measurement. An extra cable was connected parallel to an NEM resonator and connected to input of the spectrum analyzer.

The output power of the spectrum analyzer was set to V_{ACrms} =315.9 mV and the DC potential was V_{DC} =7.5 V. Up to 600 MHz, between 30 % and 60 % of the signal is transmitted, while for higher frequencies the signal is strongly reduced (figure 5.8b). Therefore characterizations of NEM resonators with a resonance frequency up to 600 MHz are possible in the low temperature setup. The measurements also showed that the impedance matching at the cryostat does reduce the electrical losses as expected [34]. The 50Ω termination at the power supply was used since it made the losses more uniform by reducing standing waves in the cables.

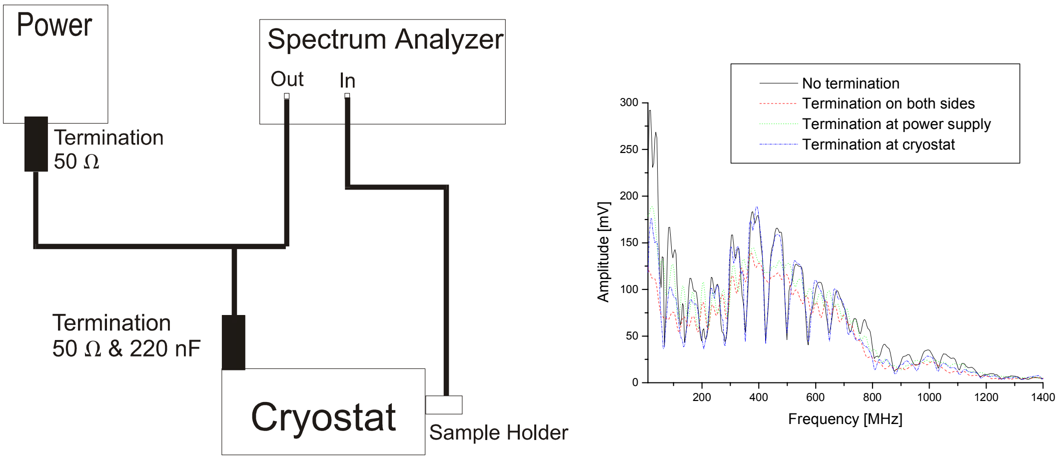

a) b)

Figure 5.8 Eelectrical calibration measurements setup (a) and results (b)

5.5.7 Temperature calibration

Since the design of the cold finger was modified, the reliability of the temperature reading needed to be checked. Therefore one sensor was mounted at the sample holder and a second sensor was clamped between two pieces of 500 µm thick silicon and two 5 mm thick copper plates. The outer copper plate was at least as close to the window as the structure during the experiment. If the two thermocouples are in equilibrium, their temperature difference is between ΔT=0.4 K at 50 K and ΔT=1.3 K at room temperature. The temperature of the sample and the sample holder are within the error range of the thermocouple above 20 K (figure 5.9b). The measurement was done without the laser, but the heating of the laser is less than one Kelvin for the silicon resonators (equation 5.4).

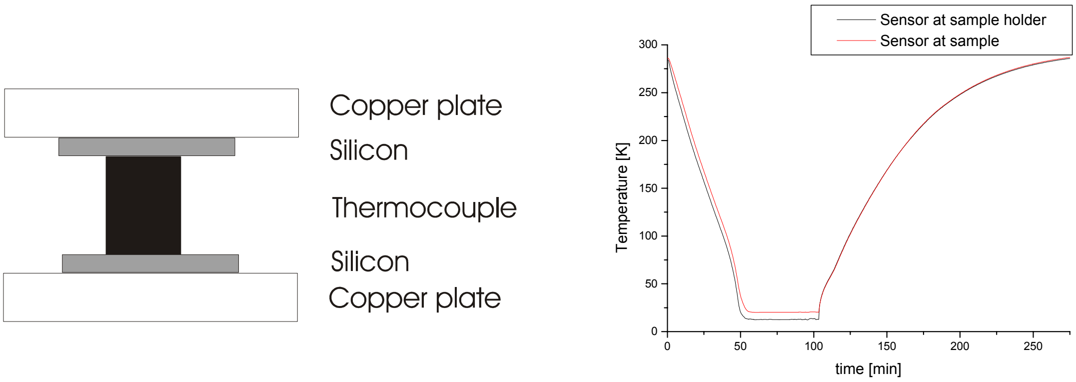

a) *b)*

Figure 5.9 Temperature calibration setup (a) and results (b)

6 Testing of nanomechanical paddle resonators

Since the nanofabrication process was not yet established at Virginia Tech, Cornell University [35] made paddle resonators available to us. The paddles used in this work are shown in figure 6.1. They had the following dimensions measures: a=200 nm, b=175 nm, L=2.5 µm, w=2 µm d=3.5 µm and an asymmetry of about d_{asym}=40 nm.

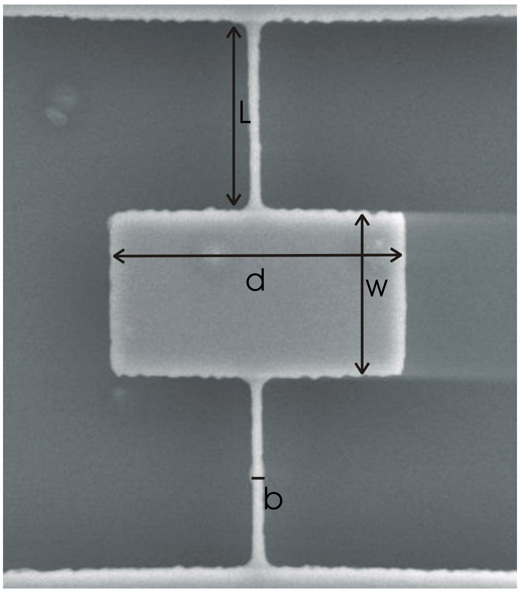

Figure 6.1 Geometry of a paddle (not visible in the picture: the thickness of the paddle a and the gap between substrate and the resonator h)

6.1 Preliminary assessment of resonant modes

6.1.1 Room temperature setup

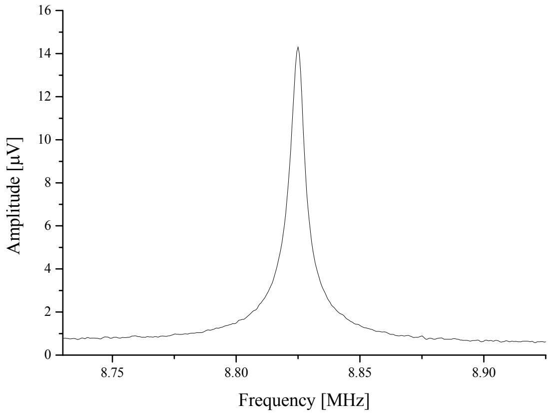

Figure 6.2 Resonance peak of room temperature measurements

To test the room temperature setup, a few resonance peaks were measured. For V_{DC}=5 V and V_{rmsAC} =315.9 mV, the resonant frequency was found at 8.96±0.05 MHz and the Q-factor was 1400±200. The pressure in the chamber was around 10 mtorr.

6.1.2 In the low temperature setup

Since the low temperature setup was equipped with a computer interface, a more detailed study of the behavior of the paddle at resonance was done. Keeping the DC potential (V_{DC}) constant and varying the AC potential affected the amplitude but not the resonant frequency nor the Q-factor. The resonant frequency was found at f_{res}=9.17 MHz with a standard derivation smaller than the resolution of the spectrum analyzer and the quality factor was found to be Q=470±70 (average over 16 measurements).

No nonlinear behavior was observed, even for larger DC potentials. The linearity can be directly seen if the detector amplitude is plotted versus the driving term (figure 6.4 a).

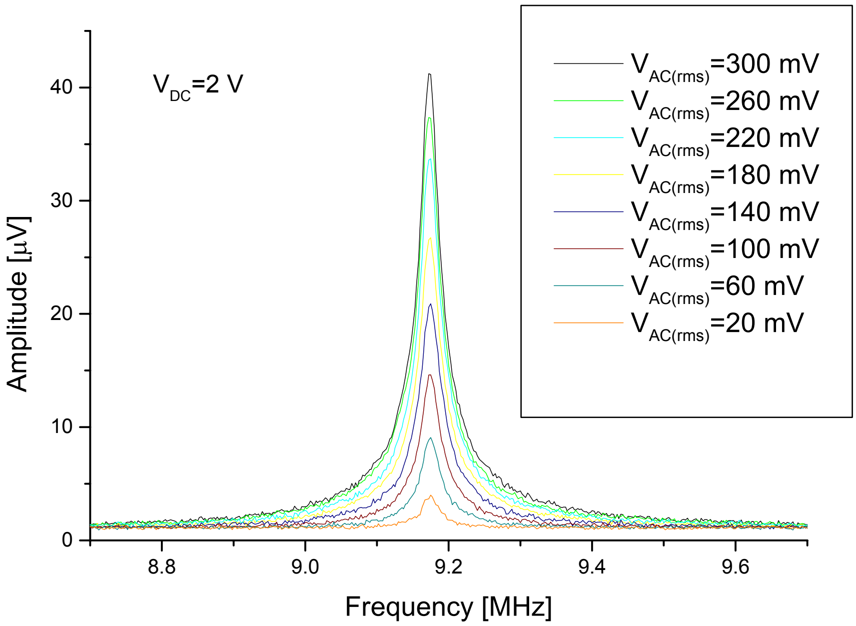

Figure 6.3 Change of Amplitude for different applied voltages (a)

From the FEM simulation, which predicted a resonance peak at 9 MHz, we can conclude that the measured mode is a superposition of a lateral and a torsional mode. Since the flexural mode of these paddle resonator are strongly non-linear [35], the torsional displacement is dominant and the lateral deflection is small.

The chamber of the low temperature setup was not an UHV chamber and had therefore a higher leak rate than the chamber of the room temperature setup. The lower quality factor is therefore due to a higher pressure in the low temperature setup, which means that the pressure in the chamber is different from the one at the vacuum gauge.

The observed difference in the resonant frequency is more difficult to explain. It is possible, but difficult, to pick up in the low frequency mode in the low temperature setup by changing the position of the stage (figure 6.3 b). Both modes are linear and have a similar Q-factor (~360). In the FEM simulation (paragraph 1.3.1) it was found that for an asymmetric paddle with an asymmetry of 10 nm different flexural modes are lying close together. Therefore the different resonant peaks are due two different torsional-translational modes, where the translational component is slightly different. Depending on the angle of the incident laser beam one or the other mode was picked up.

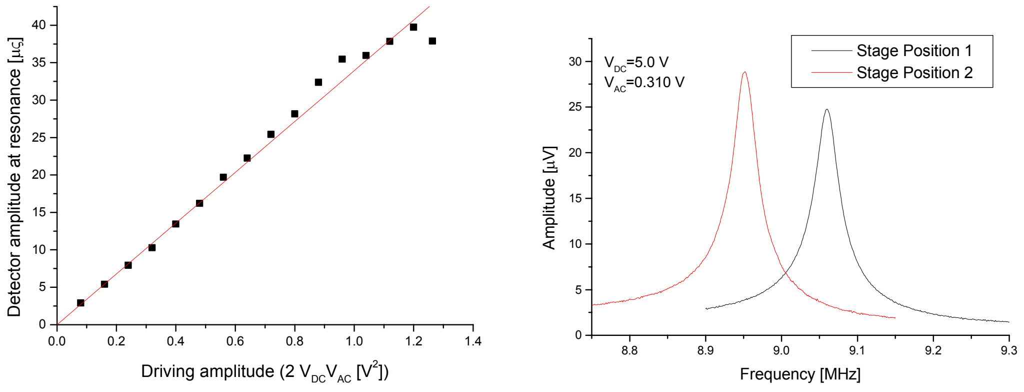

a) b)

Figure 6.4 Detector output at resonance versus driving term (a) and he resonance peak of two different modes (b)

6.2 DC dependence measurements

As derived in paragraph 2.3.2 a DC dependence of the resonant frequency is expected for the torsional mode. This dependence was found as (equation 2.89),

$$f = f_0\sqrt{1-\frac{F_{paddle}d^2}{6\kappa h}V_{DC}^2} \qquad 5.19$$

To test the influence of the DC potential on the resonant frequency experimentally, the oscillating term 2 V_{DC} V_{AC} was kept constant while the DC term was varied.
The experimental data (figure 6.5) were fitted to the equation 5.19 in the following form

$$f = f_0\sqrt{1-\alpha\frac{d^2}{6h}V_{DC}^2} \qquad 5.20$$

which leads to f_0=(9.174±0.001) MHz and α=(5.6±0.7), since

$$\alpha = \frac{F_{Paddle}}{\kappa} \qquad 5.21$$

the force conversion factor can be calculated if the torsional constant is known.

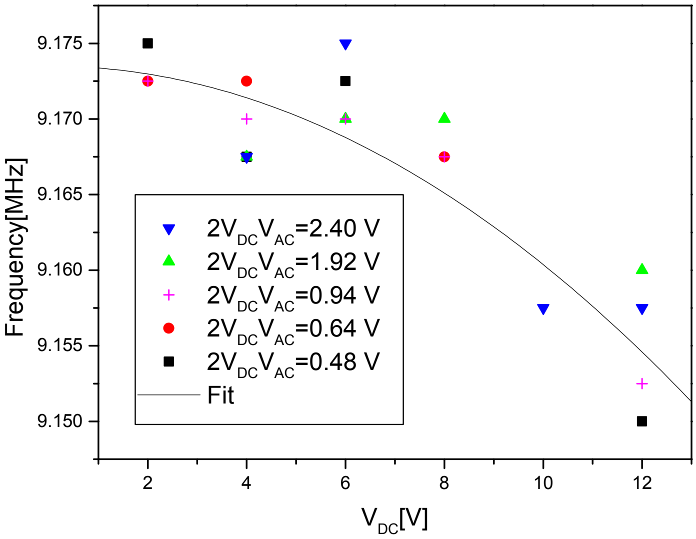

Figure 6.5 Frequency dependence on the applied DC potential

The torsional constant for a solely torsional mode can be estimated from the measured resonant frequency with

$$\kappa_{\exp} = I_{total}\left(\frac{\mathrm{f}_{res}}{2\pi}\right)^2 \tag{5.22}$$

where I_{total} is the moment of inertia of the paddle

$$I_{total} = I_{paddle} + 2I_{beam} = \frac{d^2}{2}\rho_{Si}dwa + \frac{a^2+b^2}{2}\rho_{Si}abL \tag{5.23}$$

The torsional constant is κ_{exp}=6.6 10^{-11} kg m^2 s^{-2}, using Q=470 and d_{asym}=40nm. The force conversion factor lies in the nano-Newton range (F_{Paddle}=3.9 10^{-10}).

From the applied potential the theoretical force conversion factor can be calculated using equation 5.9

$$\left|F_{Paddle}\right| = \frac{1}{2}\frac{\varepsilon_0 A}{h^2} \qquad 5.24$$

The theoretical force conversion factor is $|F_{\mathrm{Paddle}}|=2.010^{-10}$ N V^{-2}, which has the same magnitude as the one determined experimentally.

6.3 Low temperature measurements

Since it was not possible to measure while the cryostat was running, the cryostat was cooled down to its minimum temperature and then turned off. Automatically one measurement after another was taken while the cryostat was heating up.

At around 125 K an increase in the resonant frequency was observed while the Q-factor seemed not to be affected. Around this temperature liquid stains could be observed on the chip. After 150K the resonant frequency decreased again and at higher temperature the liquid stains disappeared again. The change in resonant frequency is therefore due to some substance melting around 125K and boiling around 150K. How the melting and the vaporization of that substance exactly affected the resonant frequency is not easily understood. Since an increase in the mass of the resonator would decrease and not increase the resonant frequency, the change of resonance frequency is not due to an absorption from the surrounding air. Beside this peak, the resonant frequency decreases with increasing temperature. This behavior is also observed by Evoy *et al* [33], but it is not fully understood yet.

A relaxation peak around 190 K can be observed. The only reliable way to determine the activation enthalpy H and the prefactor τ_0 of the relaxation time is by plotting lnω versus $(kT_{\max})^{-1}$. $T_{\max}$ is the temperature at the relaxation peak and ω the resonant frequency. The activation enthalpy H is then the slope and the intersection with the lnω axis is the logarithm of the prefactor $\tau_{0.}$ Therefore the activation enthalpy of this peak is not determined. But the peak is at a similar position as measured by Evoy *et al* on the same sample [33] and is not observed in macroscopic resonators [80].

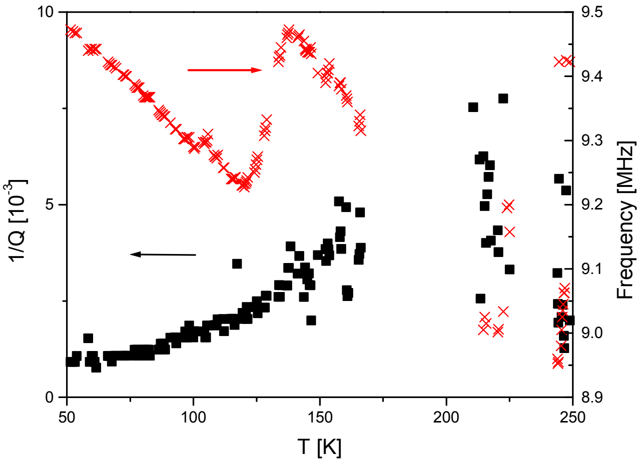

Figure 6.6 Temperature dependence of Q-factor and frequency

It is interesting to note, that for temperature below 150 K it was much easier to get reliable and reproducible measurements. The paddle reaches the same quality factor as for the room temperature setup at very low temperature (~60K). This indicates that the pressure at these low temperatures is similar to the room temperature setup. Which means that the cold finger of the cryostat acts as cryogenic pump at low temperatures. This also explains why the height of the relaxation peak measured in this experiment is much higher than the one measured by Evoy *et al* [30].

6.4 Conclusion

Sub nanometer vibration of a torsional-translational mode was measured with this setup. The measured resonant frequency agrees with the one predicted by the FEM simulation. Since no translational mode was dedected it might be possible that the setup did not pick up the vibration as a Fabry-Perot interferometer, but simple that the tilted paddle reflected part of the light away from the detector. Forces in the nano Newton regime can be detected with a torsional paddle resonator. However a better vacuum is needed to make reliable temperature dependent measurement. This and other possible improvements of the setup are discussed in chapter eight.

7 Rhodium NEMS

As mentioned in the introduction, the problem of integrating NEMS in IC-circuit are not solved yet. In this chapter a method of electrofluidic assembly of NEMS on an IC circuit will be described. The resonator itself can then be fabricated in a different step and placed on an IC device fabricated with optical lithography. This method allows also to expand the materials used for NEM resonators to materials that are not compatible with lithographical fabrication methods. In sensor applications, this method would allow the covering of all surfaces with the active sensor material and not just the top surface of the resonator, which would increase the sensitivity of the sensor.

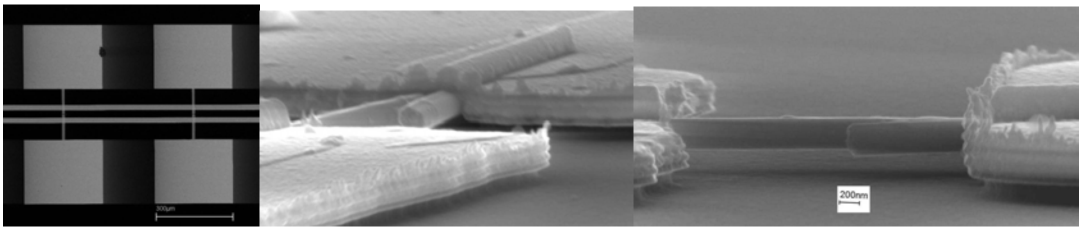

a) b) c)

Figure 7.1 Rhodium NEMS

7.1 Fabrication and assembly

The rhodium samples were fabricated in collaboration with Pennsylvania State University [73] and Ben Hailer. In the following a brief review of the fabrication process is given. A detailed description of the fabrication process of the rhodium rods is given in reference [74] and a description of the assembly of the device in reference [75].

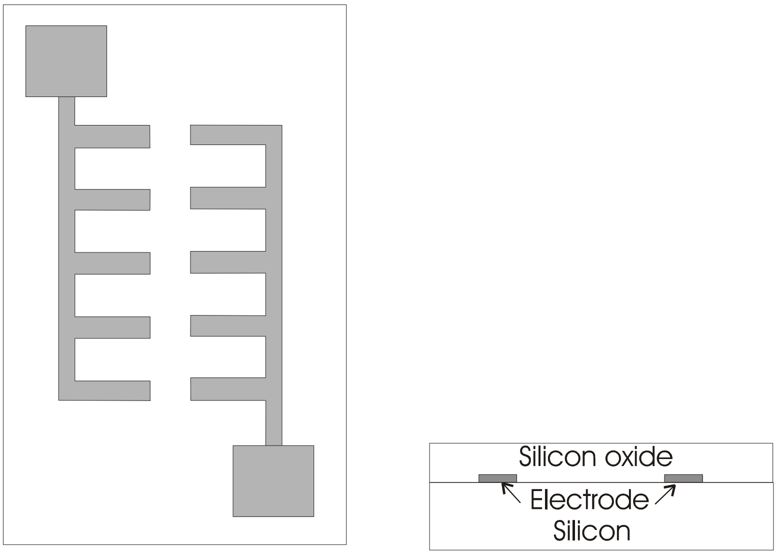

Figure 7.2 Top- and cross-sectional views of the electrodes structure

The rods were fabricated by first thermally evaporating 150 nm silver on one side of an anodized aluminum membrane (Whatman Anodisc). The pore size (240 to 450 nm) of the membrane defines the diameter of the rods. More silver was deposited galvanostatically to fill pinhole defects of the evaporated layer. The sidewalls of the pores close to the surface are often defective, so approximately 10 μm of silver was deposited inside the pores. Rhodium was than electroplated into the pores in an ice cooled ultrasonic bath. With a current density of 1.2 mA/cm^2 approximately 2.5 μm of rhodium was deposited in 90 minutes. The rhodium rods were released by dissolving the silver in 5 M nitric acid and the alumina in 5 M NaOH. After the rods were rinsed they were diluted in isopropanol.

On an oxidized silicon chip gold electrodes were defined lithographically and then protected with an additional layer of 300 nm silicon oxide (figure 7.2). To place the rods onto the electrodes an alternating electric field was applied between these electrodes. The field had a frequency of 1 kHz with an amplitude of 35 V_{rms}. The rods orientate themselves in the directions of the strongest E-field, which is between the two electrodes. The electric field decreases locally if one rod is deposited between two electrodes, therefore just a single rod is deposited on most of the electrodes.

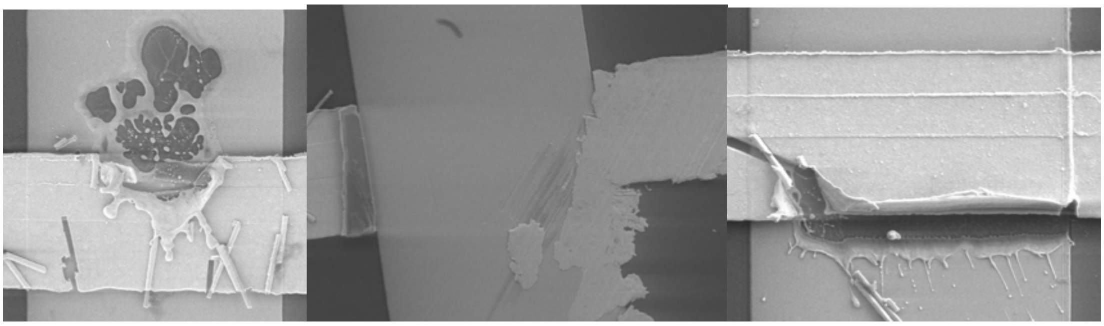

a) b) c)

Figure 7.3 Destroyed electrodes

After the isopropanol was evaporated, the bonding pads was defined lihografically and than 10 nm titanium and 500 nm gold were deposited on the chip to function as a bonding pad. The bonding pad also functioned as rigid support for the beams. In the final step the beams were released by etching the underlying 300 nm SiO_2 in buffered oxide etch (10:1 HF). The etch time was varied from 20s to 90s. It turned out that at an etch time of 20 s the beam was already released. Since the relative dielectric constant of SiO_2 is larger than one, the SiO_2 layer should increase the force on the rod (equation 5.9).

The device was now ready for wirebonding to the sample holder. The buried electrodes used during the assembly were used to ground the device. It turned out that wirebonding of rhodium samples is difficult because at a sample temperature above 100^oC wirebonding damages or even destroys the electrode between the bonding pads (figure 7.3). For temperatures between 50^oC and 80^oC it is possible to wirebond without destroying the electrode.

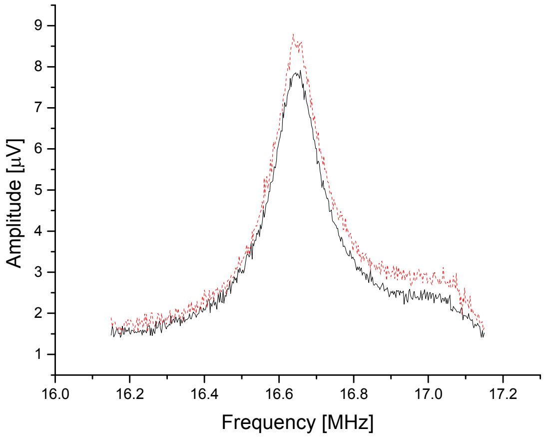

Figure 7.4 Measured resonance peaks, due to vibration of the bonding pad

7.2 Nanomechanical testing of rhodium NEMS

The characterization of the rhodium NEMS was done in the low temperature setup. We found a resonance peak in one of the samples at 16.6 MHz with a Q-factor around 160. The beam was 2.3 µm long and 350 nm in diameter. The theoretical resonance frequency should be around 220 MHz (equation 3.46). Due to the big discrepancy between theory and experiment the peak is not due to the rhodium NEM resonator, but due to the under etched gold electrode moving. That we were only able to detect this peak on a device where the electrode underneath the wired bonding pad was grounded confirms this assumption.

7.3 Discussion

Several issues may have prevented the measurement or excitation of the vibration of the rhodium NEM resonators. Compared to the silicon beams the rhodium beams had a circular cross section. This means that the light is scattered in all directions and not reflected directly back to the detector. The area where the laser beams reflected from the surface and reflected from the substrate are parallel is reduced. Since parallel surfaces are required for interference to occur, this further reduces the signal. The extinction coefficient of rhodium is k_{Rh}=5.64, a 300 nm thick beam, therefore the resonator would only transmit 2.6 x 10^{-15} of the incident light, which makes interference impossible. But also the bonding pad is opaque, whose vibration we where able to pick up. This again confirms that our experimental system not only picks vibration with Farby-Perot interferometry but that the change of the reflectance angle changes the signal enough to detect vibration.

Since the resistivity of silicon is relatively high it is more likely that the force does not act between the beam and the substrate underneath, but directly between the electrode and the beam. Due to the large distance between the electrode and the beam the force is neglectably small (400 times smaller, compared to an electrode underneath the beam).

For a 3 μm long beam with a diameter of 300 nm k_{eff}=50.1, which is a factor of 3.5 smaller than for a silicon double clamped beam, whose resonant frequency is already measured with a similar setup [76]. But since the rhodium NEM resonators are polycrystalline structures, the quality factors compared to crystalline silicon resonators is smaller. Also the clamping losses are expected to be higher since for the silicon NEMS the support and the beam is one piece, while the rhodium NEMS are clamped between a layer of SiO_2 and a gold layer, which means that microslip can occur, especially at the support edges, where the SiO_2 is etched away. The vibration amplitude is therefore smaller than for a silicon NEM resonator.

7.4 Outlook

By depositing an additional electrode underneath the beam the problem with the bad electrical grounding can be overcome. The relative dielectric constant of SiO_2 is 3.9. A remaining SiO_2-layer on the electrode would therefore increase the force on the beam compared to an air gap. Hence just enough SiO_2 to release the beam should be removed. Increasing the thickness of the bonding pad can reduce the clamping losses. Since rhodium is a relatively good conductor it also would be worth trying the magnetic detection method to detect the vibration (paragraph 5.4.2).

8 Improvements of the Setup

In this chapter recommendations are made for the improvement of the nanomechanical test setup developed in this work. Such improvements would allow more thorough research on surface-related loss mechanisms.

8.1 Optical

Alignment of the laser beam was difficult due to the inability to precisely align each part. A micrometer precise alignment in all three translational directions is recommended. Larger lenses would reduce the observed edge effects. The absorption coefficient of the optical parts used in this setup was comparably high, using parts with less absorption would increase the signal at the detector, which would result in the ability to detect even smaller vibrations. The size of the smallest device whose vibration can be detected is limited by diffraction. If the size of the resonators would be further reduced, it might be necessary to reduce the wavelength. Reducing the wavelength would have another advantage; the extinction coefficient of rhodium would be reduced to $k_{Rh}=3.1$ for violet light, which would result in a higher signal (for silicon k would increase to $k_{Si}=0.3$).

A big improvement in the quality of the setup would be achieved by using optical fiber to transport the signal to the structure and pick it up again. Such fiber would make the XYZ stage unnecessary, because the fiber itself could easily be moved to illuminate the sample. The chamber can than be screwed directly to the optical table which would reduce the vibration of the chamber. Concerns are raised that detecting a signal with optical fiber might already fail when the size of the device becomes much smaller than the diameter of the fiber, which would be long before the diffraction limit [17]. Before employing this method the theoretical resolution limit has to be calculated.

8.2 Electrical

The noise had the same level than the smallest detectable signal, to increase the sensitivity of the setup the noise should be therefore reduced. This could probably be accomplished by grounding the whole chamber and all of the equipment. As stated earlier, the power supply acted as an antenna, so a filter that cuts out all AC signals between the power supply and the rest of the system might be necessary. The noise could be further reduced if shielded cables, were also used in the vacuum chamber. A better conducting substrate would further decrease the electrical losses and could be achieved by doping the wafer from its backside. Also a metalized bonding pad would decrease the electrical losses while the resonator itself should be left without metal to obtain a high quality factor.

8.3 Room temperature setup

While the pressure in the room temperature setup was low enough to eliminate air friction, a better vacuum is needed to study surface related loss mechanisms. The better vacuum would reduce absorption and desorption at the surface.

Since it has no moving parts, an ion pump would be the best choice to obtain a higher vacuum. Not only does it not vibrate but it can also be used as a vacuum gauge. The higher limit of the working pressure of an ion pump can be obtained with a regular rotary pump. A diffusion pump that also has no vibrating parts is not a good choice since back streaming oil can contaminate the sample. To decrease the pump down time an additional turbo pump can be used. This would also allow starting the ion pump at a lower pressure, which means that the ion pump could run longer in the non-saturated mode, where the pumping speed is much higher. If the chamber is baked out overnight a vacuum of 10^{-8} torr could easily be obtained, but even lower pressures should be possible.

If the system is vented with argon the pump down time can be reduced, because it terminates the surfaces of the chamber better than nitrogen and therefore reduces the amount of water that condenses on the surfaces when they are exposed to air.

To make sure that the effective pumping speed at the sample is not drastically reduced, the Teflon spacer should have large holes, or better yet, be replaced by a metal cross that is soldered to the chamber walls. The vacuum gauge should be mounted directly in the chamber. The sensitivity to vibration can be reduced if a vacuum cross is used, where one outlet is directly screwed to the base plate.

An integrated sample heater would be helpful to remove all the water on the sample and also to look into the behavior at higher temperatures, which could reveal further relaxation peaks. A sample heater that can reach temperatures up to 200° C can be implanted relatively easily at low cost (less than $ 200). Higher temperatures would be possible but would need some more changes to the setup. The ability to reach higher temperatures (>>800^{0}C) would allow annealing the device in the vacuum chamber and making measurements without exposing it to air between treatment and measurement. If the chamber has a flow controlled inlet for processing gasses, it would be possible for example to terminate the surface with H_2 by annealing it in an H_2 atmosphere. Also, in situ measurement during an oxidation process might be possible.

8.4 Low temperature setup

The quality of the temperature dependent measurements can be increased if the cryostat were to run during the measurement. However the cryostat must not introduce any vibration into the sample, which requires either a liquid flow cryostat or a mechanical decoupling between the cold finger and the displacer. Closed cycle cryostats where the cold finger is mechanically decoupled from the displacer would reduce the vibration of the sample to 3-5 nm [77]. This displacement should be small enough to allow measurements while the cryostat is left on. The major advantage of this system is that no liquid helium is consumed during the operation which reduces the operation costs drastically. In addition, due to the decoupling of the sample from the chamber, measurements can be done with a running turbo pump, which makes an ion pump unnecessary. The advantage of a liquid flow cryostat is that temperatures down to 1.4 K can be easily achieved if He^3 is used, while the temperature of most closed circuit cryostats is limited to 10 K. For most cryostats a higher temperature option is available where temperatures up to 800 K can be attained. This would allow the characterization of a sample at the full temperature range without exposing it to air.

It is very crucial to have a high vacuum before the cool down processes starts, because otherwise the cold finger acts as a cryogenic pump and the pressure would change with temperature.

8.5 New detection method

For measuring the vibration of higher frequencies with a smaller amplitude than the one of the paddle resonator, another detection method is needed. A technique based on a scanning tunneling microscope (STM) can be used to measure the vibration of an NEM resonator. In an STM, the tip is approximately 10 Å away from the sample and if the separation between the sample and tip changes, by an angstrom, the tunnel current changes by an order of magnitude [11], which leads to the high resolution of an STM. If an STM-tip is placed above a resonator, the tunnel current should change with the position of the tip. To measure a tunneling current a DC bias has to be applied between the tip and resonator. This bias has to have the same magnitude as the DC potential used to excite the structure, so a tunnel current might already be measurable if the tip is grounded, otherwise it might be necessary to ground the resonator itself and apply the oscillating potential to excite the resonator to the substrate. Since this method needs no laser, the sample does not heat up during measurements and the experiment can also be done in the inner of a vacuum chamber far away from a viewing port, which enables measurements at even lower temperatures.

9 Conclusion and further work

This project had three objectives: The first objective was to setup an electron beam lithography tool and to develop a nanofabrication process. The second was to review existing vibration models and to develop an adequate model of the vibration of NEM resonators. The third objective was to develop a test setup for temperature-dependent experimental testing of NEM resonators.

In chapter two, after reviewing the fundamentals of vibration, an adequate model for the translational mode was described. In chapter three and four the loss mechanism of NEM resonators has been reviewed. Electron beam lithography and the fabrication process of silicon NEMS have been described in the first quarter of chapter five. The first nanostructure was fabricated as part of this work (figure 5.1a). Since the emphasis of this work was to develop a test setup for temperature dependent experimental testing of NEM resonators the rest of chapter five was dedicated to the setup. Different detection methods have been compared and then the actual setup has been described. The successful detection of sub-nanometer vibration and the dependency of the quality factor on temperature has been reported in chapter six. In chapter seven a new fabrication approach for NEM resonators using electrofluidic assembly was introduced and the first characterization attempts have been discussed. In chapter eight improvements of the existing setup have been suggested.

9.1 Further work

Since an additional relaxation peak can be observed in NEM resonators compared to macroscopic resonators, it is most likely that this peak is due to surface related losses, but its more specific origin has not yet been determined.

Other materials that have a more stable surface, might be used to obtain higher Q-factors, but these materials have the big disadvantage that they cannot easily be integrated to standard IC-fabrication processes. Therefore, besides the aspect of surface science, from a technology point of view it is beneficial to work on the understanding of loss mechanisms of silicon NEMS, because only with an understanding of underlying loss mechanism it is possible to design high quality NEM resonators.

For the experimental studies, cantilever resonators seem to be the best choice. Paddle resonators have the advantage that they produce a larger signal due to their larger size, but for simpler structures, like a double clamped beam or a cantilever, it is much easier to model their resonance behavior or their loss mechanisms. This allows a better comparison between experiment and theory. Cantilevers are preferable over double clamped beams due to their larger resonance amplitude, which makes it easier to pick up their vibration. It is further preferable to space the cantilever so that just one cantilever is measured at a time. With harp structures [73], for example, it is not possible to differentiate between the higher mode of a shorter beam and the fundamental mode of a larger beam. To obtain a comprehensive understanding of the relevant loss mechanism, the temperature should be varied not only from 50 K to room temperature, but from at least 1.4 K [59] to almost the melting point of the material. Further the experiments must be done with several resonators resonating at different frequencies.

The first step to an understanding of surface related loss mechanisms is to know the surface properties of the resonator. The surface roughness can be obtained with an AFM, which might be difficult, since the structure might start moving in contact with the AFM tip. To learn something about the contamination on the surface, spectroscopy methods can be used. How the fabrication process has damaged the crystal structure in the near surface region can be investigated with cross section transmission electron microscopy.

If the surface composition is known, these parameters can be varied. One of the first experiments that should be done is to remove the silicon oxide layer and all impurities on the surface and then make temperature dependent measurements of the resonator. The next step would be measurements on resonators with different oxide layer thicknesses. Other interesting experiments would be measurements on resonators with different surface roughness or amounts of surface impurities. Also the effect of the 10 nm thick water layer that condenses on the silicon surface should be investigated.

Besides experimental studies, a theoretical understanding of these loss mechanisms is also needed. So far not much theoretical work on the loss mechanisms on NEMS has been done and all of the work is related to the fundamental loss mechanisms [42], which will finally limit the achievable Q-factor, but they are not the dominant loss mechanism in today’s devices. Due to the difficulty of developing an analytical model for surface related loss mechanisms, it might be helpful to simulate the behavior of the surface and near surface region. Atomistic simulations have been used to understand energy dissipation that occurs if a crack proceeds in a cast niobium aluminide intermetallics [15]. The same kind of simulation might be helpful to understand energy dissipation of NEM resonators.

From a technology point of view the integration of NEMS with ICs will be a major obstacle to overcome. The methods used to integrate MEM devices have not been demonstrated yet to work for NEM devices. A new technique might be to use surface acoustic waves (SAW) to pick up the resonance. The feasibility of this method was already demonstrated [62] but a more detailed investigation is necessary.

Bibliography

[1] R P. Feynman, “There's plenty of room at the bottom” American Physical Society Meeting (Pasadena, CA), 1960 (www.its.caltech.edu/~feynman)

[2] D. M. Eigler, E. K. Schweizer, Nature 344, 524 (1990)

[3] D. Bimberg, M. Grundmann, N.N. Ledentsov, Quantum Dot Heterostructures, Wiley 1999

[4] M. C. Cross, R. Lifshitz, Phys. Rev. B 64, 085324 (2001)

[5] J. W. Gardner, V. K. Varadan, O. O. Awadelkarim, Microsensors MEMS and Smart devices, Wiley 2001

[6] M. J. Madou, “LIGA and other replication techniques”, in the MEMS Handbook, CRC Press 2002

[7] T. Ujiie, A. Yamazaki, M. Watanabe, T. Okuda, T. Ichiki, Y. Horiike, Digest of Papers Microprocesses and Nanotechnology (IEEE Cat. No.00EX387), 28 (2000)

[8] K. Grenier, D. Dubuc, L. Rabbia, A. Tackac, P. Pons, T. Parra, P. Caudriller, H. Aubert, J. Graffeuil, O. Pascal, P. Combes, H. Baudrand, R. Plana, Proceedings of the Fourth IEEE International Caracas Conference on Devices, Circuits and Systems, 202 (2002)

[9] H. J. De Los Santos, Introduction to Microelectromechanical Microwave Systems, Artech House Publishers, 1999

[10] Li Fan, A. Husain, P. D. Dobblelaere, S. Gloeckner, S. Patra, S. Gutierrez, P. Marchand, C. King, T. Yeh, Y. Loke, J. Hartman, J. Gritters, 14th Annual Meeting of the IEEE Lasers and Electro-Optics Society (Cat. No.01CH37242), 10 (2001)

[11] A practical guide to scanning probe Microscopy, Park Scientifig Instrument

[12] J.-S. Park, C. Wilson, Y. B. Ginachandani Micromechanical pressure sensors, in the MEMS Handbook, CRC Press 2002

[13] B. Ilic, D. Czaplewski, H. G. Craighead, P. Neuzil, C. Campagnolo C. Batt, Appl. Phys. Lett. 77, 450 (2000)

[14] A. Erbe, G. Corso, H. Kroemmer, A. Kraus, K. Richter, and R.H. Blick, Appl. Phys. Lett. 77, 3102 (2000)

[15] F. Ye, D. Farkes, W.O. Soboyejo, Mat. Sci. Eng. A 264, 81 (1999)

[16] A. A. Ayon, Microfabrication for MEMS Part IV: Case analysis and concsions, in Symposium Tutorial at 2001 MRS fall meeting, Boston

[17] M. L. Roukes, Phys. World 14, February 2001

[18] A. N. Cleland and M. L. Roukes, Nature 392**,** 160 (1998)

[19] H. J. Mamin, D. Rugar, Appl. Phys. Lett. 79 (2001) 3358

[20] R. H. Blick, A. Erbe, A. Tilke, A. Wixforth, Phys Bl 1, 31 (2000)

[21] M. L. Roukes, Sci. Am. 285, 48 (1998)

[22] G. Genta, Vibration of Structure and Machines , Springer 1999

[23] H. A. C. Tilmans, M. Elwenspoek, J. H. J. Fluitman, Sens. and Actuators A 30, 35 (1992)

[24] A. A. Shabana, “Vibration of Discrete and Continuous Systems” Springer-Verlag 1997

[25] D. W. Carr, Nanoelectomechanical Resonators, Ph.D. thesis Cornell University 2000

[26] S. Rast, C. Wattinger, U. Gysin, E. Meyer, Revi. Sci. Instrum. 71, 2772 (2000)

[27] P. C. Chou, NJ Pagano: Elasticity, Tensor, Dyadic and engineering approaches, Dover Publication 1992

[28] E. Goens, Ann. Physik 5, 42 (1931)

[29] G. Pickett, Proceedings ASTM 45, 846 (1945)

[30] e1875-00e1 Standard Test Method for Dynamic Young's Modulus, Shear Modulus, and Poisson's Ratio by Sonic Resonance, ASTM International 2002

[31] A. N. Cleland, M. L. Roukes, Sens. and Actuators 72, 256 (1999)

[32] A. A. Shabana, “Theory of Vibration Volume I” Springer-Verlag 1990 and G. Mack, lecture notes: “Klassische Mechanik” Universitaet Hamburg 1997-2000

[33] S. Evoy, A. Olkhovets, L. Sekaric, J. M. Parpia, H. G. Craighead , D. W. Carr, Appl. Phys. Lett. 77 (2000), 2397

[34] A. Olkhovets, Nano Electro Mechanical Systems and their applications, Ph.d. Thesis Cornell 2001

[35] S. Evoy, D. W. Carr, L. Sekaric, A. Olkhovets, J. M. Parpia, H. G. Craighead, J. Appl. Phys. 86, 6072 (1999)

[36] E. H. Dowell, D. Tang , J. Appl. Phys. 90, 5606 (2001)

[37] The simulations were done by Christopher Maxey on ANSYS 5.7.1

[38] K. Wang, A. C. Wong, C. T. C. Nguyen, J. Microelectromech. Syst. 9, 347 (2000)

[39] R. D. Biggar and J. M. Parpia, Rev. Sci. Instrum. 69, 3558 (1998)

[40] M. Alonoso, E. J. Finn, Physics, Addison-Wesley 1992

[41] B. Purniah in T.V. Ramakrishnan, M. R. Lakshmi, Non-Debye Relaxation in Condensed Matter , World Scientific Singapore 1987

[42] R. Lifshitz, M. L. Roukes, Phys. Rev. B. 61, 5600 (2000)

[43] F. R. Blom, S. Bouwstra, M. Elwenspoek, J .H. J. Fluitman, J. Vac. Sci. Technol. B 10, (1992) 19

[44] H. Hosaka, K. Itao, S. Kuroda, Sens. and Actuators A 49, (1995) 87

[45] Y. H. Cho, A. P. Pisano, R. T. Howe., J. Microelectromech. Syst. 3, (1994) 81

[46] Z. Osinikis, Damping of vibrations, A. A. Balkema 1998

[46] D. A. Harrington, P. Mohanty, M. L. Roukes, Phys. B 248-288, 2145 (2000)

[47] V. B. Braginskey, V. P. Mitrofanov, V. I. Panov, Systems with small dissipation, The University of Chicago Press 1985

[48] V. Palmov, Vibration of Elasto-Plastic Bodies, Springer-Verlag 1998

[49] R. De Batist, Internal friction of structural defects in crystalline solids, North-Holland Publishing Company, 1972

[50] A. S. Nowick, B.S. Berry, Anelastic relaxation in Crystalline Solids, Academic Press 1972

[51] C. Zener, Phys. Rev. 52, 230 (1937)

[52] C. Zener, Phys. Rev. 53, 90 (1938)

[53] C. Zener, W. Otis, R. Nuckolls, Phys. Rev. 53, 100 (1938)

[54] R. Lifshitz, submitted to Elsevier Science, 2001

[55] T. S. Ke, Metallurgical and Materials Transaction A 30A, 2267 (1999)

[56] T. S. Ke, Phys. Rev. 71, 553 (1947)

[57] T. S. Ke, Phys. Rev. 72, 41 (1947)

[58] K. Y. Yasumura, T. D. Stowe, E. M. Chow, T. Pfafman, T.W. Kenny, B. C. Stipe, D. Rugar, J. Microelectromech. Syst. 9, 117 (2000)

[59] B. E. White, R. O. Pohl, Phys. Rev. Let. 75, 4437 (1995)

[60] S. Evoy, A. Olkhovets[2], D. W. Carr, J. M. Parpia[2], H. G. Craighead, Mat. Res. Soc. Symp. Proc. Vol. 657, EE1.3.1 (2001)

[61] J. Yang, T. Ono, M. Esashi, J. Vac. Sci. Technol. B 19, 551 (2001)

[62] F. W. Beil, A. Wixforth, R.H. Blick to be published

[63] M. A. McCord, M. J. Rooks in P. Rai-Choudhury "Handbook of microlithography, micromachining and microfabrication", p. 139, SPIE Optical Engineering Press 1997

[64] W. T. Barnhart, Development of Nanoelectromechanical Resonators for RFIC Applications, Thesis Virgina Tech. 2002

[65] D.W. Carr, H. G. Craighead, J. Vac. Sci. Technol. B 15, 2760 (1997)

[66] Personal communication with Fred A. Mahone from the physics electronic shop, 2002

[67] R. H. Blick, A. Erbe, H. Krömmer, A. Kraus, J. P. Kotthaus, Phys. E 6, 821 (2000)

[68] A. N. Cleland, M.L. Roukes, Sens. and Actuators 72, 256 (1999)

[69] E. Buks, M.L. Roukes, Europhys. Lett. 54, 2220 (2001) and E. Buks, M.L. Roukes, Phys. Rev. B. 63, 033402 (2001)

[70] Private communication with David E. Oliver from Polytec, 2002

[71] R.C. Crafere, P.J. Oakley, Laser processing in manufacturing, Chapman & Hall 1993

[72] E. Hecht, Optics, 3rd Edidtion, Addison-Wesley Longman, Inc. 1998

[73] S. Evoy, B. Hailer, M. Duemling, B.R. Martin, T. E. Mallouk, I. Kratochvilova, T.S. Mayer, to appear in Mat. Res. Soc. Symp. Proc. (2002)

[74] B. R. Martin, D. J. Dermody, B. D. Reiss, M. Fang, L. A. Lyon, M. J. Natan, T. E. Mallouk, Advanced Material 11, 1021 (1999)

[75] P. A. Smith, C. D. Nordquist, T. N. .Jackson, T. S. Mayer, B. R. Martin, J. Mbindyo, T. E. Mallouk, Appl. Phys. Lett. 77, 1399 (2000)

[76] D.W. Carr, S. Evoy, L. Sekaric, H. G. Craighead HG, J. M. Parpia, Appl. Phys. Lett. 75, 920 (1999)

[77] Product information of Advanced Research Systems, Inc.

[78] W. A. Zdaniewski, G. E. Rindone, D. E. Day, J. Mat. Sci. 14, 763 (1979)

[79] M. Scherge, X. Li, J.A Schaefer, Tribol. Lett. 6, 215 (1999)

[80] S. V. Starodubtsev, D. Kaipnazarov, L. P. Khizinichenko, P. F. Kromer, Sov. Phys. Solid State (Engl Transl) 8, 1521 (1966)

Vita

Martin Duemling was born on June 3rd, 1975 in Muellheim, Germany. In 1995 he graduated from Markgraefler Gymnasium Muellheim, Germany. After his civil service at the Red Cross in Muellheim he went to the University of Hamburg, Germany, where he studied physics and received his Vordiplom in October 1999. In 2000 he joined Virginia Tech as graduate student.

Martin will have completed the requirements of the degree of Masters of Science in Material Science Engineering in August 2002.